Source Terms in a Third-Generation Wind Wave Model*

HENDRIK L. TOLMAN AND DMITRY CHALIKOV+

Ocean Modeling Branch, Environmental Modeling Center, NOAA/NCEP, Camp Springs, Maryland

(Manuscript received 5 January 1995, in final form 20 May 1996)

ABSTRACT

A new third-generation ocean wind wave model is presented. This model is based on previously developed input and nonlinear interaction source terms and a new dissipation source term. It is argued that the dissipation source term has to be modeled using two explicit constituents. A low-frequency dissipation term analogous to wave energy loss due to oceanic turbulence is therefore augmented with a diagnostic high-frequency dissipation term. The dissipation is tuned for the model to represent idealized fetch-limited growth behavior. The new model results in excellent growth behavior from extremely short fetches up to full development. For intermediate to long fetches results are similar to those of WAM, but for extremely short fetches the present model presents a significant improvement (although the poor behavior of WAM appears to be related to correctable numerical constraints). The new model furthermore gives smoother results and appears less sensitive to numerical errors. Finally, limitations of the present source terms and possible improvements are discussed.

1. Introduction

Modeling of the sea state has been in the center of interest for half a century. After the pioneering work of Gelci et al. (1956), ocean wave models are generally based on a spectral energy or action balance equation. In the past two decades international cooperation in measurement and modeling projects like JONSWAP (Hasselmann et al. 1973), SWAMP (SWAMP Group 1985), and SWIM (SWIM Group 1985) has greatly increased our knowledge of the evolution of such wave spectra. This focused research culminated in the development of the WAM model (WAMDIG 1988). This model is the first so-called third-generation model, in which a spectral balance equation is integrated without predefined spectral constraints. This approach has lead to a model that is applicable in a broad range of wave conditions, ranging from day-to-day average wave conditions to hurricane conditions (see WAMDIG 1988). It furthermore allows for model improvements at the elementary level of the parameterizations of the physics involved. Previous first and second generation models leaned heavily upon assumed effects of the physics. This implies that such models generally require implementation-specific tuning and can generally be improved only by retuning.

The essential processes governing wave growth are all present in the relatively simple case of fetch-limited growth in deep water without currents. In such conditions, the balance equation for the two-dimensional variance density spectrum of surface elevations $F(f, \theta)$ can be written as

$$\frac{\partial F}{\partial t} + \mathbf{c}_g \cdot \nabla_{\mathbf{x}} F = S_{\text{wind}} + S_{\text{nl}} + S_{\text{ds}}, \qquad (1)$$

$$c_g = \frac{\partial \omega}{\partial k}, \quad \omega^2 = gk,$$

where $f\,(=\omega/2\pi)$ and θ are the spectral frequency and direction, respectively; k is the spectral wavenumber; and S_{wind}, S_{nl}, and S_{ds} represent source terms for wind–wave interactions (also denoted as the input S_{in}), resonant wave–wave interactions, and dissipation, respectively. For convenience of notation, the dependence of the F and S on f and θ has been neglected. The WAM model originally used parameterizations of Snyder et al. (1981), Hasselmann et al. (1985), and Komen et al. (1984) for the above three source terms (see WAMDIG 1988). More recently, Janssen (1989, 1991), Snyder et al. (1992), and Burgers and Makin (1993) have proposed alternative source term parameterizations, and Janssen's modifications have been implemented in the most recent release of WAM (cycle 4). Modifications mostly concentrate on replacing the empirical formulation of S_{wind} of Snyder et al. (1981) by more rigorous parameterizations. The dissipation source term S_{ds}, however, has not been studied in detail. This source term represents the least known part of the balance equation (1) and is generally used as the clo-

* Ocean Modeling Branch Contribution Number 122.
\+ UCAR Visiting Scientist.

Corresponding author address: Dr. Hendrik L. Tolman, Ocean Modeling Branch, Environmental Modeling Center, NOAA/NCEP, 5200 Auth Road, Room 209, Camp Springs, MD 20746.

sure term to tune WAM to represent predefined fetch-limited growth behavior.

The present paper presents an alternative set of source terms. Our wind–wave interaction source term (section 2) is based on Chalikov and Belevich (1993), and is similar to S_{wind} as used by Burgers and Makin (1993). The nonlinear interactions (section 3) are described using the discrete interaction approximation (DIA) of Hasselmann et al. (1985), as is used in WAM. In developing our (new) dissipation source term in section 4, we conclude that the dissipation processes for frequencies around and below the spectral peak are fundamentally different from those in the equilibrium range of the spectrum. The latter high-frequency dissipation applies to a part of the spectrum that carries only a small fraction of the total wave energy. It nevertheless needs to be modeled explicitly to avoid that high-frequency dissipation processes dictate the spectral shape of the dominant low-frequency dissipation term. We therefore divide the dissipation source term in two constituents: In the low-frequency regime, we assume that S_{ds} can be described using an analogy with dissipation of wave energy due to oceanic turbulence. A diagnostic parameterization for the high-frequency dissipation was obtained by assuming a quasi-steady balance of source terms in the corresponding regime. The resulting dissipation source term has several tuneable parameters. These parameters have been estimated by optimizing fetch-limited growth behavior (section 5). The resulting growth behavior is illustrated and discussed in section 6.

2. Wind–wave interaction

Computations of the statistical structure of the wave boundary layer above monochromatic and multimode surfaces, based on the 2D Reynolds equations (Chalikov 1980; Burgers and Makin 1993; Chalikov and Belevich 1993), indicate that the wind–wave interaction source term S_{wind} can be parameterized as

$$S_{\text{wind}}(f, \theta) = \beta\omega F(f, \theta), \tag{2}$$

where β is a nondimensional wind–wave interaction parameter, which can be approximated as

$$10^4\beta = \begin{cases} -a_1\tilde{\omega}_a^2 - a_2, & \tilde{\omega}_a \leqslant -1 \\ a_3\tilde{\omega}_a(a_4\tilde{\omega}_a - a_5) - a_6, & -1 < \tilde{\omega}_a < \Omega_1/2 \\ (a_4\tilde{\omega}_a - a_5)\tilde{\omega}_a, & \Omega_1/2 < \tilde{\omega}_a < \Omega_1 \\ a_7\tilde{\omega}_a - a_8, & \Omega_1 < \tilde{\omega}_a < \Omega_2 \\ a_9(\tilde{\omega}_a - 1)^2 + a_{10}, & \Omega_2 < \omega_a, \end{cases} \tag{3}$$

where

$$\tilde{\omega}_a = \frac{\omega u_\lambda}{g}\cos(\theta - \theta_w) \tag{4}$$

is the nondimensional frequency of a spectral component, θ_w is the wind direction, and u_λ is the wind velocity at a height equal to the "apparent" wavelength

$$\lambda_a = \frac{2\pi}{k|\cos(\theta - \theta_w)|}. \tag{5}$$

The parameters $a_1 - a_{10}$ and Ω_1, Ω_2 in Eq. (3) depend on the drag coefficient C_λ at the height $z = \lambda_a$:

$$\begin{aligned} \Omega_1 &= 1.075 + 75C_\lambda, \\ \Omega_2 &= 1.2 + 300C_\lambda \\ a_1 &= 0.25 + 395C_\lambda, \\ a_2 &= 0.35 + 150C_\lambda, \\ a_3 &= (a_0 - a_2 - a_1)/(a_0 - a_4 + a_5) \\ a_4 &= 0.30 + 300C_\lambda, \\ a_5 &= a_4\Omega_1 \\ a_6 &= a_0(1 - a_3) \\ a_7 &= (a_9(\Omega_2 - 1)^2 + a_{10})/(\Omega_2 - \Omega_1) \\ a_8 &= a_7\Omega_1 \\ a_9 &= 0.35 + 240C_\lambda, \\ a_{10} &= -0.05 + 470C_\lambda, \\ a_0 &= 0.25a_5^2/a_4. \end{aligned} \tag{6}$$

The behavior of the interaction parameter β has been discussed in detail by Chalikov and Belevich (1993), and is illustrated in their Fig. 1. The main features of the present source term compared to empirical relation of Snyder et al. (1981) are: (i) It becomes negative for waves traveling at large angles with the wind or faster than the wind. In such conditions the dynamic pressure of the wind on the forward face of the wave component exceeds the pressure on the backward face, resulting in an energy flux from the waves to the wind. (ii) It results in a 2 to 3 times smaller integral input of energy for fully grown seas. This is partially due to the negative growth rates of overdeveloped wave components and due to relatively small growth rates for wave components near full development. (iii) At high frequencies it results in a larger energy input than Snyder's relation because for $\tilde{\omega}_a > 2$, β of Eq. (3) is proportional to $\tilde{\omega}_a^2$. This also implies that the differences in integral input between the present source term and Snyder's relation becomes considerably smaller for young waves. Note that the input of WAM cycle 4 is also significantly smaller than the Snyder et al. relation for mature waves (Komen et al. 1994, Fig. 3.2).

The energy flux from waves to wind is not present in previous parameterizations of the input source term and has several potential impacts compared to nonnegative input parameterizations. (i) It might result in a more narrow spectrum because the wave components propagating under large angles with the wind obtain

less energy and even may lose it. (ii) Similarly, negative input is expected to influence the response of the spectrum to changes in wind direction. (iii) The loss of energy for low-frequency waves might slow wave growth for well-developed spectra and thus might contribute to the reaching of an equilibrium between source terms. (iv) The negative energy flux in the low-frequency range is accompanied by a weakening of the momentum flux from air to the sea. For sufficiently developed wave spectra the sea surface may therefore become very smooth.

The above approximation of β was compared with observations of β collected by Plant (1982) in Chalikov and Belevich (1993, Fig. 2). It was shown that scatter of the data can be explained by the dependence of β on C_λ. The data also exhibits the quadratic dependence of β on $\tilde{\omega}_a$ for large $\tilde{\omega}_a$. Note, however, that it is extremely difficult to obtain dependable observations of β, because of the difficulties of measuring the energy flux to waves (Panchenko and Chalikov 1984; Chalikov and Makin 1990). The resulting scatter in observed growth rates makes a direct validation of input source terms virtually impossible (e.g., Hasselmann and Bösenberg 1991).

In the present source term the values of u_λ and C_λ are assigned at a height equal to the apparent wavelength λ_a. Because the wind velocity and drag coefficient change with height, introduction of u_λ and C_λ eliminates the uncertainty in choosing an arbitrary reference level, which is inherent to all previous schemes for evaluating β. This reduces the number of governing parameters and follows the physics involved because the thickness of the layer in which wind–wave interaction takes place becomes thinner with increasing frequency (decreasing λ).

Because the wind is usually defined at a given height (h), u_λ and C_λ need to be derived as part of the present parameterization of S_{wind}. It is well established now that an overwhelming part of the wave-produced momentum flux is formed in the high-frequency part of the spectrum that is not resolved in most wave models. The only way to take into account the form drag of the waves therefore is to use an effective roughness parameter z_0. Its value depends on the energy of high-frequency wave components and for a JONSWAP spectrum is connected to the Phillips parameter α by the relation

$$z_0 = \chi \alpha^{1/2} \mathcal{L}, \tag{7}$$

where $\mathcal{L} = u_*^2/g$ is the Charnock scale, and χ is a constant ($0.15 < \chi < 0.25$, we use $\chi = 0.2$ in our calculations) and u_* is the friction velocity in air. Equation (7) can be considered as a generalization of Charnock's relation (Charnock 1955) taking into account the sea state. Excluding a thin surface layer adjusting to the water surface, the mean wind profile is close to logarithmic

$$u_z = \frac{u_*}{\kappa} \ln\left(\frac{z}{z_0}\right), \tag{8}$$

where $\kappa = 0.4$ is the von Kármán constant. Combined with Eq. (7) this expression can be rewritten in terms of a drag coefficient $C_z = u_*^2/u^2(z)$

$$C_z = \kappa^2 (R - \ln(C_z))^2, \tag{9}$$

where

$$R = \ln\left(\frac{zg}{\chi\sqrt{\alpha} u^2}\right) \tag{10}$$

is a nondimensional parameter (see Chalikov and Belevich 1993). To complete the present parameterization of S_{wind}, an estimate for α is needed. Such an estimate could be obtained directly from the wave model. However, such estimates are known to be somewhat unstable. Furthermore, the relevant part of the spectrum is often outside the discrete frequency range of the spectrum. Alternatively, α can be estimated parametrically from other parameters supplied by the wave model. Following Chalikov (1995), C_z can be estimated from the phase velocity c_p at the spectral peak frequency f_p as

$$C_z = \exp(0.074 R_1 + 0.2345 \ln(R_1) - 6.783). \tag{11}$$

$$R_1 = \frac{u^2}{gz}\left(\frac{u}{c_p}\right)^{3/4}. \tag{12}$$

This approximation completes our input source term. For a given wind speed u and direction θ_w at height h the algorithm for the calculation of S_{wind} thus becomes:

1) Calculate C_h from Eqs. (12) and (11), estimating c_p from the wave model.

2) Calculate z_0 from the drag coefficient C_h. Using Eq. (8) and the definition of C_h, z_0 becomes

$$z_0 = h \exp(-\kappa C_h^{-1/2}). \tag{13}$$

3) Calculate the apparent wave length λ_a using Eq. (5).

4) Calculate the wind speed u_λ and drag coefficient C_λ as

$$u_\lambda = u_h \frac{\ln(\lambda_a/z_0)}{\ln(h/z_0)} \tag{14}$$

$$C_\lambda = C_h \left(\frac{u_h}{u_\lambda}\right)^2. \tag{15}$$

5) Calculate the nondimensional frequency $\tilde{\omega}_a$ from Eq. (4).

6) Calculate β as function C_λ and $\tilde{\omega}_a$ using Eqs. (3) and (6).

7) Calculate the source term form Eq. (2).

3. Nonlinear interactions

The calculation of the nonlinear interactions formally requires the evaluation of a six-dimensional

Bolzmann integral, the computational effort of which greatly exceeds economical limits for operational wave models. Because the nonlinear interactions are generally recognized to play a crucial role in the process of wave growth (e.g., Hasselmann et al. 1973), several attempts have been made to develop economical parameterizations of S_{nl} (see Hasselmann et al. 1985). In spite of this effort, only one economical parameterization has proved adequate for application in a third-generation wave model. This is the discrete interaction approximation (DIA), developed by Hasselmann et al. (1985). The DIA as implemented in WAM considers mirror-symmetrical discrete interaction configurations of four wavenumber vectors, where $\mathbf{k}_1 = \mathbf{k}_2$ and $\mathbf{k}_1 + \mathbf{k}_2 = \mathbf{k}_3 + \mathbf{k}_4$. Resonance conditions then require the following relation between the corresponding frequencies

$$\omega_2 = \omega_1$$
$$\omega_3 = (1 + \mu)\omega_1$$
$$\omega_4 = (1 - \mu)\omega_1, \qquad (16)$$

where μ is a constant $0 < \mu < 1$. The contribution $\delta S_{nl,n}$ to the source term S_{nl} at the wavenumber $\mathbf{k}_n$ in the above resonance configuration is calculated analogous to the exact interactions as (cf. WAM)

$$\begin{pmatrix} \delta S_{nl,1} \\ \delta S_{nl,3} \\ \delta S_{nl,4} \end{pmatrix} = D \begin{pmatrix} -2 \\ 1 \\ 1 \end{pmatrix} C g^{-4} f^{11} \left[F_1^2 \left(\frac{F_3}{(1+\mu)^4} + \frac{F_4}{(1-\mu)^4} \right) - \frac{F_1 F_3 F_4}{(1-\mu^2)^4} \right], \qquad (17)$$

where $F_n \equiv F(f_n, \theta_n)$, C is a numerical constant, and D is a scaling factor to account for limited water depth (expression not reproduced here). Note that Eq. (17) implies a logarithmic distribution of frequencies and an isotropic distribution of directions in the discrete spectrum as used in WAM [see Eq. (5.5) of Hasselmann et al. (1985)]. The evaluation of (17) for resonance configurations close to the highest and lowest discrete frequencies in the spectrum requires spectral information outside the discrete spectral range. For frequencies lower than the lowest discrete frequency $F(f, \theta) = 0$ is assumed. For frequencies higher than the high-frequency cutoff f_c, a power-law type spectrum is assumed:

$$F(f, \theta) = F(f_c, \theta) \left(\frac{f}{f_c} \right)^{-m}, \qquad (18)$$

where m is typically assumed to be 4 to 5. We will use $m = 5$, for which the one-dimensional spectrum $\mathcal{F}(f) = \int_\theta F(f, \theta) d\theta$ corresponds to the JONSWAP spectrum. Equation (17) is evaluated for $\mathbf{k}_1$ corresponding to each discrete combination (f, θ) in the discrete spectrum of the wave model and for some additional high frequencies, for which the interaction contributions at $\mathbf{k}_4$ fall within the discrete spectral space. The actual source term is obtained by summation of all resulting contributions.

This source term is tuned by selecting a number of values for μ and corresponding values for C. As suggested by Hasselmann et al. (1985), WAM uses a single interaction configuration defined by $\mu = 0.25$ and $C = 2.8 \times 10^7$. In this configuration, the DIA proved successful as demonstrated by Hasselmann et al. (1985) and by several years of successful operation of many implementations of the WAM model. It does not, however, reproduce the exact nonlinear interaction precisely, as is illustrated in Fig. 7 of Hasselmann et al. (1985). The shift of energy to low frequencies is fairly accurately described, but the DIA significantly overestimates interactions at frequencies above the spectral peak frequency. This results in broader spectra with higher energy levels in the equilibrium range (Hasselmann et al. 1985, Figs. 8 and 12). It furthermore has a noticable impact on the spectral shape as will be illustrated below. To reduce the impact of the errors of the DIA at high frequencies, its strength has been reduced ($C = 1 \times 10^7$). This corresponds to a more even distribution of errors over the spectral domain. Effects of this rescaling are discussed in section 7.

4. Dissipation

The dissipation source term describes loss of wave energy due to wave breaking ("whitecapping") and turbulence in the oceanic boundary layer. The description of such processes in the energy balance equation (1) is not straightforward, as both are discontinuous and incorporate rotational motion contrary to other processes in (1). Furthermore, the process of wave breaking and its governing parameters are still poorly understood. The dissipation source term is thus the least known term in the balance equation, and is mostly used as a tunable closure term.

Several parameterization for the dissipation source term have been proposed. A review is given by Donelan and Yuan (1994). Such source terms generally assume that a single dissipation parameterization can be applied throughout the spectrum. This dissipation source term $S_{ds}(f, \theta)$ is assumed to be quasi-linear in terms of the spectrum $F(f, \theta)$, because small changes in the details of the spectral shape of swell or of the peak of a wind sea spectrum cannot be expected to influence the integral dissipation $\int\int S_{ds}(f, \theta) df d\theta$ significantly. Introducing a dissipation timescale T_{ds}, the source term becomes

$$S_{ds}(f, \theta) = T_{ds}^{-1} F(f, \theta), \qquad (19)$$

where T_{ds} can be a function of the spectral coordinates f and θ, environmental parameters like u_*, and mean wave parameters. These arguments appear solid for frequencies around or below the spectral peak frequency.

For higher frequencies, however, observations and similarity considerations suggest the existence of a self-similar shape of the one-dimensional frequency spectrum $\mathcal{F}(f)$. This implies a quasi-steady equilibrium of source terms (and advection), suggesting that T_{ds} is a function of the wave energy in a limited range of the spectral space. As the high-frequency shape of the spectrum furthermore is at best a weak function of the fetch, mean wave parameters are not expected to significantly influence T_{ds} in the equilibrium range.

The above timescales for the spectral peak and lower frequencies (denoted below as low frequencies) and for the equilibrium range (denoted as high frequencies) are obviously incompatible. The dissipation source term therefore has to consist of (at least) two constituents. The parametric high-frequency tail, which in WAM is applied for numerical reasons (''disparities in response timescales,'' WAMDIG 1988), might seem a simple way to account for high-frequency dissipation separately. However, a parametric tail fixes the shape of the spectrum, but not the high-frequency energy level α. This level then can only be influenced by the frequency dependency of the explicit dissipation source term. High-frequency dissipation thus still influences the shape of the low-frequency dissipation. To avoid this ''cross-contamination,'' the high-frequency dissipation should be described explicitly (see also Banner and Young 1994).

Our present knowledge of wave energy dissipation is clearly insufficient to firmly define the two dissipation constituents. In this study, we will somewhat arbitrarily assume that the low-frequency dissipation has a form similar to the energy dissipation due to turbulent viscosity in the oceanic boundary layer (section 4a). Note that a turbulent dissipation term has been suggested before by Duffy and Huang (oral presentation at the eighth WAM meeting, Geneva Park, Canada, 1990). Our parameterization for high-frequency dissipation (section 4b) is purely diagnostic and is designed to be consistent with the occurrence of a power-law behavior of the equilibrium range. In section 4c the combination of these two constituents is discussed.

a. Low-frequency dissipation

A consistent approach to parameterize turbulent dissipation of wave energy (Kitaigorodskii and Miropolskii 1968; Benilov and Lozovatskii 1977; Phillips 1977; Kitaigorodskii and Lumley 1983) is based on representing velocity and pressure fields in the Navier–Stokes equations as a sum of mean, potential (wave), and turbulent components. If wave motion and turbulence are not correlated, their interaction can be accounted for by introducing an effective turbulent viscosity coefficient K, which is a function of the vertical coordinate z. This ''eddy viscosity'' reduces the kinetic energy of the waves, and it is assumed that a mechanism of mutual adjustment exists between the potential and kinetic wave energy.

A local rate of total kinetic wave energy dissipation can be calculated as (Kitaigorodskii and Miropolskii 1968)

$$\left\langle \frac{K}{2}\tilde{\Phi}_{ij}\tilde{\Phi}_{ij}\right\rangle = 2g\int\int K(z)k^3F(f,\theta)e^{-2kz}dfd\theta, \tag{20}$$

where the summation convention is used and where $\Phi_{ij} = \partial\tilde{u}_i/\partial x_j + \partial\tilde{u}_j/\partial x_i$ is the strain tensor of the orbital wave velocity $\tilde{u}$; angle brackets denote averaging over time (or horizontal coordinates) to account for the entire wave field. A spectral dissipation equivalent to (20) requires integration over depth and is given as

$$S_{ds,l}(f,\theta) = 2k^3F(f,\theta)\int_0^\infty K(z)e^{-2kz}dz. \tag{21}$$

Because most wave energy dissipation occurs in the mixed layer of the ocean, effects of stratification of the water column can be neglected. Dimensional considerations then suggest that the vertical profile $K(z)$ can be represented as

$$K(z) \sim u_*h\tilde{K}\left(\frac{z}{h},\xi\right), \tag{22}$$

where $\tilde{K}$ is a nondimensional eddy viscosity, h is a bulk mixing length scale, and ξ is a nondimensional parameter describing the development stage of the wave field (typically the nondimensional peak frequency f_pu_*/g or the nondimensional energy Eg^2/u_*^4). Considering that the momentum and energy fluxes from the atmosphere to the ocean are concentrated in the high-frequency part of the spectrum, the bulk mixing scale h is estimated as the equivalent wave height of the high-frequency part of the spectrum

$$h = 4\left(\int_0^{2\pi}\int_{f_h}^\infty F(f,\theta)dfd\theta\right)^{1/2}, \tag{23}$$

where f_h is a frequency significantly higher than the peak frequency of the windsea part of the spectrum (see section 4c). Introducing (22) into the integral in (21), the effective eddy viscosity K_e becomes

$$\begin{aligned} K_e &= k\int_0^\infty K(z)e^{-2kz}dz \\ &= u_*h\int_0^\infty k\tilde{K}\left(\frac{z}{h},\xi\right)e^{-2kz}dz = u_*h\phi(\xi), \end{aligned} \tag{24}$$

where ϕ is a nondimensional function, which will be estimated in section 5. The effective eddy viscosity thus depends on the momentum transport from the atmosphere to the ocean (u_*), the energy of high-frequency waves (h), and on the development stage of the wave field [$\phi(\xi)$]. The latter will allow for an indirect way of accounting for the change of the ratio of the mixing

length scale h to the penetration depth of the wave motion and for different "whitecap" intensities at different stages of the wave growth. Substituting (24) in (21), the low-frequency dissipation source term then becomes

$$S_{ds,l}(f, \theta) = -2u_* hk^2 \phi(\xi) F(f, \theta). \quad (25)$$

Note that this dissipation disappears in the absence of wind ($u_* = 0$) and/or high-frequency waves ($h = 0$) and hence is indirectly but strongly linked to the input source term.

b. High-frequency dissipation

Presently, wave energy dissipation for high frequencies is poorly (if at all) understood, and no attempts have been made to explicitly formulate this energy dissipation. Moreover, the entire source term balance for this part of the spectrum is less well known than that for low frequencies, because neither the wind–wave interaction parameter β (Chalikov and Belevich 1993; Burgers and Makin 1993), nor the nonlinear interactions according to the DIA (section 3) are well established in this spectral regime. We will therefore define a diagnostic high-frequency dissipation, designed to result in a consistent source term balance for $f \to \infty$ when combined with our other source terms. For simplicity, the timescale T_{ds} will be assumed to be directionally isotropic. To be consistent with the parametric tail needed to calculate S_{nl} [Eq. (18) with $m = 5$], the high-frequency dissipation should result in the corresponding one-dimensional frequency spectrum

$$\mathcal{F}(f) = \alpha g^2 (2\pi)^{-4} f^{-5}, \quad (26)$$

which corresponds to a Phillips or JONSWAP type spectrum. To guarantee that the high-frequency dissipation can result in such a spectral shape, we assume that the timescale T_{ds} depends nonlinearly on α;

$$T_{ds}^{-1} = A[\alpha_n(f)]^B, \quad (27)$$

where $\alpha(f) = \mathcal{F}(f) f^5 g^{-2} (2\pi)^4$ is the frequency-dependent nondimensional energy level, normalized with some universal representative energy level α_r, and where expressions for A and B still are to be determined. This formulation is equivalent to a nonlinear dependence of the source term on the local steepness $k^2 \mathcal{F}(f)$ and can therefore be loosely interpreted as a local (in f-space) application of the dissipation source terms as presently used in WAM.

The required form of A and B can be determined from the spectral energy balance (1) at high frequencies. Considering that effects of propagation are irrelevant for the high frequencies considered here, and integrating over the spectral directions, Eq. (1) implies

$$\int_\theta S_{ds,h}(f, \theta) \approx -\int_\theta S_{wind}(f, \theta) - \int_\theta S_{nl}(f, \theta). \quad (28)$$

The source terms, and hence the timescales, scale with the wind friction velocity u_*. Defining the timescale for arbitrary source terms S as $T^{-1} \equiv \int_\theta S d\theta / \int_\theta F d\theta$, the nondimensional timescale $\tilde{T}_{d,h} \equiv T_{d,h} g / u_*$ becomes

$$\tilde{T}_{ds,h}^{-1} \approx -\tilde{T}_{wind}^{-1} - \tilde{T}_{nl}^{-1}. \quad (29)$$

The inverse timescale of the wind input scales with $\omega\beta$ [Eq. (2)], which for high frequencies corresponds to f^3. The inverse timescale of the nonlinear interactions scales with $f^{11} F^2$ [Eq. (17)], which in the tail corresponds to f. The right side of Eq. (29) thus is dominated by the input term for sufficiently high f, in which case

$$\tilde{T}_{ds,h}^{-1} = -\tilde{T}_{wind}^{-1} = -a_0 \tilde{f}^3, \quad (30)$$

where a_0 is a constant depending on the directional distribution in the tail only and where the nondimensional frequency $\tilde{f} = f u_* g^{-1}$. However, contributions of the nonlinear interactions to Eq. (29) are generally not negligible in the high-frequency range explicitly considered by a numerical wave model (roughly $2f_p < f < 3f_p$). For several JONSWAP spectra with the directional distribution of Hasselmann et al. (1980) this is illustrated in Fig. 1. Following modeling customs, the directional distribution is kept constant for $f > 2.5 f_p$. For increasing f_p, $\tilde{T}_{nl}^{-1}$ increases as α increases with f_p and $\tilde{T}_{nl}^{-1}$ scales with α^2 (within the parametric tail). This dependence of the importance of the nonlinear interactions on f_p and α suggests the following expression for the timescale of the high-frequency dissipation

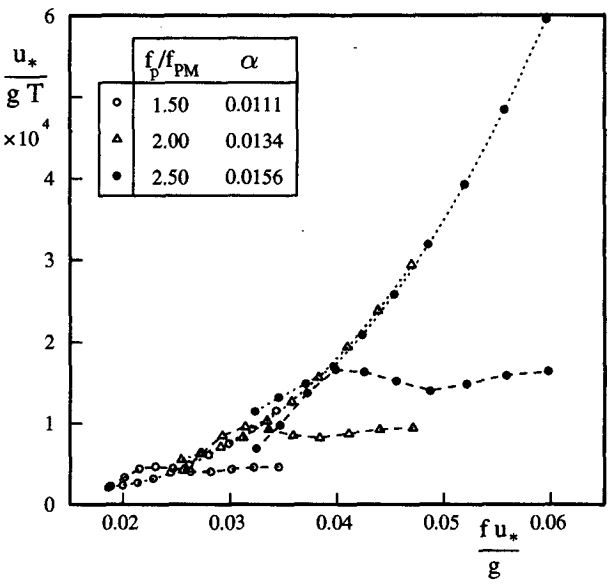

FIG. 1. Inverse nondimensional timescales $\tilde{T}^{-1} = u_*/(gT)$ as a function of the nondimensional frequency fu_*/g for the input source term (dotted lines) and the nonlinear interactions (dashed lines) for several JONSWAP spectra with the directional distribution of Hasselmann et al. (1980). Results for $1.75 < f/f_p < 4$ only.

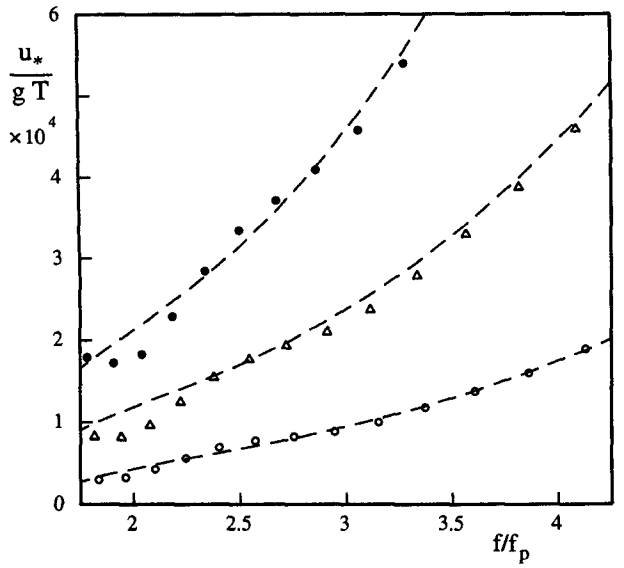

FIG. 2. Inverse nondimensional timescales $u_*/(gT)$ as a function of the nondimensional frequency f/f_p according to Eq. (29) (symbols) and Eq. (31) with $a_0 = 2.7$, $a_1 = 0.0017$, $a_3 = 2$, and $\alpha_r = 0.008$ (dashed lines). Legend as in Fig. 1.

$$\tilde{T}_{\mathrm{ds},h}^{-1} = -a_0 \tilde{f}^3 [\alpha_n(f)]^B, \quad B = a_1 \tilde{f}^{-a_2}, \quad (31)$$

where a_0, a_1, a_2 and the normalization energy level α_r have to be determined by tuning (see section 5). The potential of this equation to describe the required dissipation timescale (29) for sufficiently high frequencies f/f_p is illustrated in Fig. 2. Using the definition of $\tilde{T}$, the corresponding source term becomes

$$S_{\mathrm{ds},h}(f, \theta) = -a_0 \left(\frac{u_*}{g}\right)^2 f^3 [\alpha_n(f)]^B F(f, \theta), \quad (32)$$

$$B = a_1 \left(\frac{f u_*}{g}\right)^{-a_2}.$$

c. Total dissipation

The total dissipation source term is defined here as a linear combination of the above high and low frequency constituents. Defining a transition zone to guarantee continuous behavior, the total dissipation becomes

$$S_{\mathrm{ds}}(f, \theta) = \mathcal{A} S_{\mathrm{ds},l} + (1 - \mathcal{A}) S_{\mathrm{ds},h}, \quad (33)$$

$$\mathcal{A} = \begin{cases} 1 & \text{for } f < f_1 \\ \dfrac{f - f_2}{f_1 - f_2} & \text{for } f_1 \leq f < f_2 \\ 0 & \text{for } f_2 \leq f, \end{cases} \quad (34)$$

where $\mathcal{A}$ is defined by the highest (f_2) and lowest frequency (f_1) of the transition zone and where $S_{\mathrm{ds},l}$ and $S_{\mathrm{ds},h}$ are given by Eqs. (25) and (32), respectively. To enhance the smoothness of the model behavior for frequencies near f_c, a similar transition zone is used between the prognostic spectrum and the parametric high-frequency tail as in Eq. (18)

$$F(f_i, \theta) = (1 - \mathcal{B}) F(f_i, \theta) + \mathcal{B} F(f_{i-1}, \theta) \left(\frac{f_{i-1}}{f_i}\right)^m, \quad (35)$$

where i is a discrete frequency counter and which is valid for nondecreasing discrete frequencies only, and where $\mathcal{B}$ is defined similarly to $\mathcal{A}$, ranging from 0 to 1 between f_2 and f_c.

Furthermore, the frequencies f_1, f_2, f_c and the integration bound f_h in Eq. (23) have to be defined. In idealized conditions such frequencies are usually defined relative to the peak frequency f_p of the spectrum (Fig. 3). For a practical wave model with multimodal seas, f_p should be the peak frequency of the windsea. Determining this frequency requires separation of swell and windsea, which is not always straightforward. A representative frequency for the peak of the windsea spectrum in complex conditions can alternatively be obtained from the input source term, which by definition covers actively growing spectral components only. The numerical experiments of the following sections have shown that the peak frequency of the wind input and f_p generally differ less than 5% for standard fetch-limited wave growth. The peak frequency, however, can still show discontinuous behavior for complex spectra, which can be avoided by considering the mean frequency of the positive part of S_{wind}. Furthermore, weighing the input with f^{-3} to bring the mean input

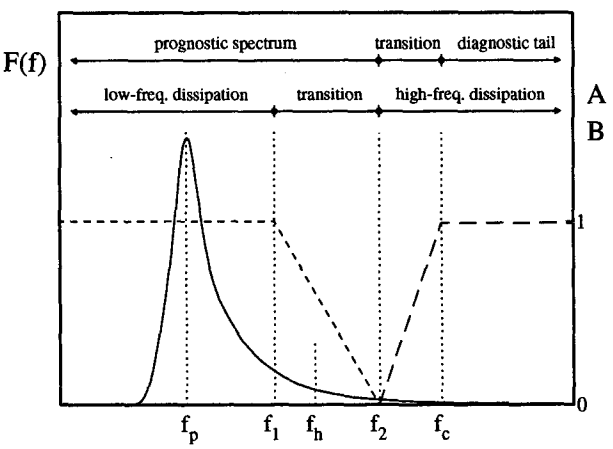

FIG. 3. Frequencies relevant to the source terms and source term integration (qualitatively) and the filter functions $\mathcal{A}$ (short dash) and $\mathcal{B}$ (long dash). The solid line represents the spectrum. f_p is the spectral peak frequency, f_c is the cutoff frequency between the deterministic part of the spectrum and the parametric tail, f_h is the integration bound in the calculation of the turbulence scale h [Eq. (23)], and f_1 and f_2 define the linear combination of low- and high-frequency dissipation.

frequency close to the spectral mean frequency [for high frequencies $\int_\theta S_{\text{wind}}(f,\theta)d\theta \propto f^3 \int_\theta F(f,\theta)d\theta$, see previous section], and defining the mean frequency as an inverse mean period for increased numerical smoothness (cf. WAM), our representative input peak frequency $f_{p,i}$ becomes

$$f_{p,i} = \frac{\iint f^{-3} \max[0, S_{\text{wind}}(f,\theta)]\,df d\theta}{\iint f^{-4} \max[0, S_{\text{wind}}(f,\theta)]\,df d\theta}. \quad (36)$$

The estimation of f_1, f_2, f_c, and f_h in terms of $f_{p,i}$ (or f_p) should be considered as a part of the tuning process. However, most frequencies can be estimated independently, and the resulting model behavior proved fairly independent of the values established below. We will use

$$\begin{aligned} f_c &= 3.00 f_{p,i} \\ f_1 &= 1.75 f_{p,i} \\ f_2 &= 2.50 f_{p,i} \\ f_h &= 2.00 f_{p,i}. \end{aligned} \quad (37)$$

Note that the integration bound f_h is meant to represent the frequency range in which the majority of the momentum transfer from atmosphere to ocean occurs. As discussed above, f_h is similar to f_c. From a numerical point of view, such an estimate of f_h is not preferred as the energy in the parametric tail tends to be noisy. It is therefore preferable to use a lower estimate of f_h. The corresponding overestimation of h is automatically compensated for in the empirical estimate of ϕ.

The peak frequency is also used in Eq. (12). Consistency requires that this relation is also expressed in terms of $f_{p,i}$. The numerical experiments of the following section resulted in the following parametric relation:

$$\tilde{f}_p = 3.6 \times 10^{-4} + 0.92\tilde{f}_{p,i} - 6.3 \times 10^{-10}\tilde{f}_{p,i}^{-3}, \quad (38)$$

which is valid for $0.008 < \tilde{f}_{p,i} < 0.04$. The first two terms on the right side dominate for short and intermediate fetches. In this regime, $f_{p,i}$ is virtually identical to the mean frequency as defined in WAM. The rightmost term represents a correction for long fetches, where the spectrum still can develop to lower frequencies, but where the peak frequency of the input becomes systematically higher than the mean frequency of the wind sea spectrum.

5. Tuning the source terms

To accommodate tuning, the present source terms have been implemented in the third-generation wind wave model WAVEWATCH (Tolman 1991, 1992). This model was implemented to represent standard fetch-limited test conditions of Eq. (1). The model has been tuned by modifying the free parameters in the dissipation source term while leaving the input and nonlinear interactions as described in sections 2 and 3. The model is tuned to optimally represent the nondimensional total energy $\tilde{E} = Eg^2 u_*^{-4}$ and the high-frequency energy level $\alpha(f_c)$ as a function of the nondimensional fetch $\tilde{x} = xgu_*^{-2}$. Scaling with u_* was selected because our source terms scale with u_*.

Observations of fetch-limited wave growth have been gathered and discussed by Kahma and Calkoen (1992, 1994). For consistency with our model, u_* should include effects of wave-generated roughness. Kahma and Calkoen (1994) present such growth curves for stable stratification of the atmospheric boundary layer, unstable stratification, and the composite dataset. The first two datasets result in the following growth curves:

$$\tilde{E} = 7.3 \times 10^{-4}\tilde{x}^{0.85}, \quad 2\pi\tilde{f}_p = 3.0\tilde{x}^{-0.26}, \quad (39)$$

$$\tilde{E} = 1.6 \times 10^{-4}\tilde{x}^{1.00}, \quad 2\pi\tilde{f}_p = 4.7\tilde{x}^{-0.30}. \quad (40)$$

Note that $\tilde{f}_p$ is not used in the tuning process and hence presents an independent check on model behavior. For the energy level α no such detailed analyses are available. We have tuned the model to

$$\alpha = 0.295\tilde{x}^{-0.22}, \quad (41)$$

which was obtained from Hasselmann et al. (1973), converting from u_{10} scaling to u_* scaling by assuming $\alpha = 0.0085$ for $\tilde{x} = 10^7$.

Due to the scaling behavior of the model, it is sufficient to tune the model for a single wind speed. We have arbitrarily selected $u_{10} = 20$ m s^{-1}. The scaling behavior, however, is potentially influenced by numerical properties of the model, that is, the spectral, temporal and spatial resolutions, and the propagation scheme (see Tolman 1992). To minimize effects of the spectral resolution, a relatively high spectral resolution has been used ($\Delta f/f = 0.08$ and $\Delta\theta = 10°$), and the discrete frequency range is chosen so that $f_{\max} > f_c$ and $f_{\min} < 0.5 f_p$ for all spatial grid points. To minimize effects of the temporal resolution, the dynamic source term integration scheme of Tolman (1992) has been used. Numerical errors related to the spatial resolution are concentrated in the first few offshore grid points. Therefore, the optimization is performed for two grids. The first consists of up to 38 points with a spatial increment $\Delta x = 25$ km, extending up to nearly full-grown conditions. For the runs tuned to the stable stratification data this includes all 38 grid points; for the unstable data it includes approximately 15 points. The second grid consists of 38 points with a spatial resolution $\Delta x = 2.5$ km, covering small fetches only. Fetch-limited growth behavior is expected to be fairly insensitive to the numerical propagation scheme (Tolman 1992, Fig. 8). To improve stability and convergence, we have used a simple first-order propagation scheme.

TABLE 1. Optimization results for the high-frequency dissipation source term (32) for the four basic test cases with $\alpha_r = 0.002$. The row identified as "points" shows the counters of the grid points used in the optimization.

	Stable stratification		Unstable stratification	
	Short fetch	Long fetch	Short fetch	Long fetch
Points	14–38	3–17	14–38	3–12
a_2	1.80	2.19	1.50	1.55

The parameters to be tuned in our dissipation source term are ϕ in Eq. (25) and a_0, a_1, a_2, and α_r in Eq. (32). Several of these parameters can be tuned objectively given the parametric growth curves for $\tilde{E}$ and α.

Because the low-frequency dissipation acts on most of the wave energy, its free function ϕ dominates the evolution of $\tilde{E}(\tilde{x})$. Therefore, a local estimate ϕ_l can be obtained for each spatial grid point by tuning $\tilde{E}(\tilde{x})$ to Eq. (39) or (40). This tuning of ϕ_l has been performed using a simple successive correction scheme (equations not presented here). A parametric description of ϕ based on the local solutions ϕ_l is determined as the last step of the optimization process.

The constant a_0 in the high-frequency dissipation (32) is defined by Eq. (30). Using the definition of the nondimensional timescale, and considering that a_0 is a function of the directional distribution in the tail only, a local estimate $a_{0,l}$ of a_0 can be calculated for every spatial grid point as

$$a_{0,l} = \tilde{f}_c^{-3} \frac{u_*}{g} \frac{\int_\theta S_{\text{wind}}(f_c, \theta) d\theta}{\int_\theta F(f_c, \theta) d\theta}. \qquad (42)$$

In the optimization, a_0 is kept constant along the fetch and is estimated as the average of the local estimate $a_{0,l}$ along the fetch.

Given the above estimate of a_0, the high-frequency behavior of the model is governed by a_1, a_2, and α_r. Optimum values for these parameters are determined by tuning the model to Eq. (41) for $f > f_c$. In this tuning process a local estimate for $a_{1,l}$ was made for preset values of a_2 and α_r. The optimum values for the latter two parameters are defined as those that resulted in the smallest spatial variability of $a_{1,l}$. The selected values for a_2 and α_r are presented in Table 1, and corresponding local estimates for $a_{0,l}$ and $a_{1,l}$ are presented in Figs. 4 and 5, respectively.

Estimates for $a_{0,l}$ in the high-frequency dissipation as presented in Fig. 4 are consistent between the long- and short-fetch runs, and show a negligible dependence on the fetch $\tilde{x}$. The results for the stable and unstable stratification data show a small but systematic difference.

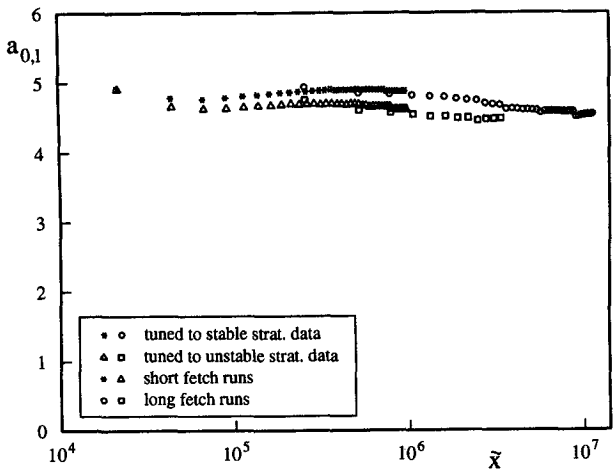

FIG. 4. Local estimates $a_{0,l}$ [Eq. (42)] of a_0 in Eq. (32) as a function of the nondimensional fetch $\tilde{x}$ for the four test cases: $\alpha_r = 0.002$, $a_2 = 2.0$ for cases tuned to stable stratification data, and $a_2 = 1.5$ for cases tuned to unstable stratification data.

Estimates for $a_{1,l}$ as presented in Fig. 5 show a much larger dependency on the fetch. In the short-fetch runs (* and △), $a_{1,l}$ drops to 0 for the smallest fetches. This occurs because the input source term is insufficiently strong to support the corresponding large values of α. For the long-fetch runs (○ and □) $a_{1,l}$ is systematically smaller for the first two grid points only. This behavior is related to numerical propagation errors. Finally, $a_{1,l}$ shows a systematic increase for the large fetches in the long-fetch run tuned to the stable stratification data (○). This behavior is related to the fact that ϕ becomes unrealistically low for fetches outside the range of applicability of Eq. (39) (see below). Because the above three regimes are showing a pronounced behavior of $a_{1,l}$ with fetch, they have been excluded from the op-

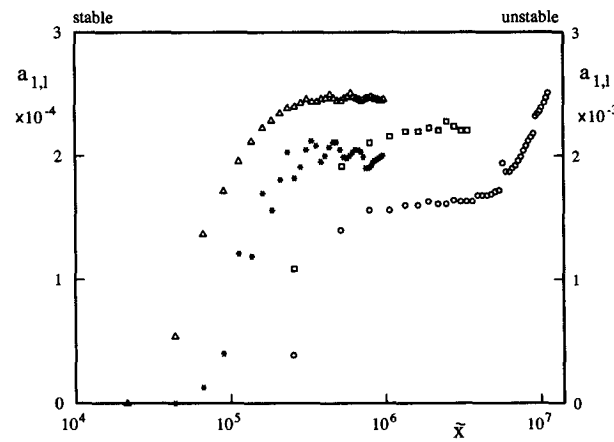

FIG. 5. Local estimates $a_{1,l}$ of a_1 in Eq. (32) as a function of the nondimensional fetch $\tilde{x}$. Legend and parameter settings as in Fig. 4.

timization of a_1 (see Table 1). For the remaining fetches, $a_{1,i}$ within the separate runs is independent of the fetch. The results for the four separate runs, however, all show significant differences.

Considering the above, it appears reasonable to estimate a_0, a_1, a_2, and α_r independent of the fetch, in accordance with the reasoning in section 4b. The optimum values do, however, depend significantly on the growth curve $\tilde{E}(\tilde{x})$ to which the model is tuned. Of the four parameters, a_1 and a_2 show a dependency on the spatial resolution and, hence, on numerical propagation errors. Below, we will neglect this influence of propagation errors and use identical estimates of the above four dissipation parameters for corresponding long- and short-fetch runs.

As the final step of the tuning process, the dissipation function ϕ in Eq. (25) is optimized locally, using the parameters for the high-frequency dissipation as gathered in Table 2. As described in section 4, ϕ will be estimated in terms of a parameter describing the development stage of the wave field. We have chosen to express ϕ in terms of the nondimensional peak input frequency $\tilde{f}_{p,i}$, which is closely related to the wave age c_p/u_*. The local optimum estimates of ϕ as a function of $\tilde{f}_{p,i}$ are presented in Fig. 6. The results for the long- and short-fetch runs are consistent, showing only small effects of numerical propagation errors. For most of the range of $\tilde{f}_{p,i}$, ϕ can be estimated using a simple linear relation

$$\phi = b_0 + b_1 \tilde{f}_{p,i}. \tag{43}$$

Corresponding values for b_0 and b_1 are given in Table 2. For the long-fetch run tuned to the stable stratification data (○ in Fig. 6), ϕ becomes systematically lower than predicted by the linear relation (43). This behavior occurs in conditions near full development, where $\tilde{f}_{p,i}$ can decrease no more because the wind–wave interaction parameter β becomes negative for the low-frequency flank of the spectrum. Similarly, the input of wave energy by wind cannot increase further. An increase of wave energy with fetch can then only be achieved by an increased rate of decrease of ϕ. This decrease of ϕ causes a corresponding increase of $a_{1,i}$ in Fig. 5. Because this behavior occurs for fetches well outside the applicability of Eq. (39), this increased reduction of ϕ cannot be realistic. It might nevertheless be useful to deviate from the linear relation (43) for conditions near full development, defining a minimum value $\phi_{\min}$ for the smallest expected value $\tilde{f}_{p,i,\min}$, as this gives us some control on establishing "full-growth" wave energies.

TABLE 2. Optimal parameter setting in Eqs. (32) and (43) obtained from tuning the model to Eqs. (39) or (40) and to Eq. (41), ($\alpha_r = 0.002$, $\tilde{f}_{p,i,\min} = 0.009$, $\phi_{\min} = 0.003$).

	a_0	a_1	a_2	b_0	b_1
Eq. (39)	4.8	1.7×10^{-4}	2.0	0.3×10^{-3}	0.47
Eq. (40)	4.5	2.3×10^{-3}	1.5	-5.8×10^{-3}	0.60

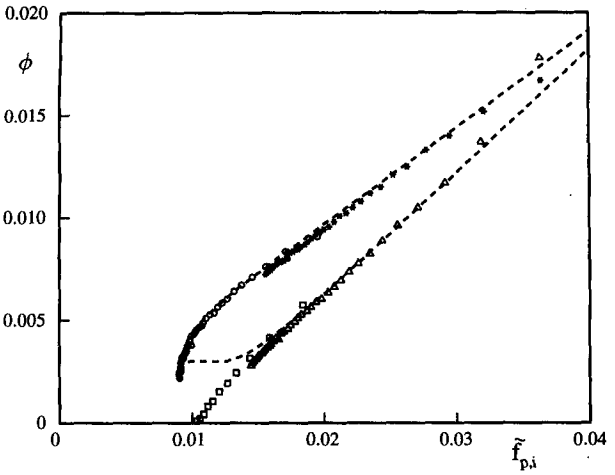

FIG. 6. The dissipation function ϕ in Eq. (25) as a function of the input peak frequency $\tilde{f}_{p,i}$. Symbols as in Fig. 4. Dashed lines: Eq. (43) with parameter values of Table 2, relaxed to $\phi_{\min}$ and $\tilde{f}_{p,i,\min}$.

For model runs tuned to the unstable stratification data (□ and △) the linear relation (43) describes all obtained values of ϕ. However, for the longest fetches ϕ goes to zero before $\tilde{f}_{p,i}$ reaches its "saturation" level. This would imply that fully developed seas correspond to a complete absence of low-frequency dissipation and is obviously not realistic. The runs tuned to the unstable stratification data therefore also suggest the establishment of a minimum value $\phi_{\min}$.

Figure 6 indicates that $\tilde{f}_{p,i,\min} \approx 0.009$. To get results for long fetches close to the Pierson and Moskowitz (1964) results, we have selected $\phi_{\min} = 0.003$. The linear relation (43) approaches the minimum values smoothly as shown in Fig. 6.

6. Results

The new source terms have been tested in several ways. First, we will present mean wave parameters and spectral details for the physical and numerical conditions for which the model has been tuned in the previous section. Second, we will assess the scaling behavior of the new model for realistic wind speeds and the presently common spectral resolution of the WAM model. Similarly, we will assess the nondimensional behavior in terms of the wind speed u_{10} (instead of u_*) and effects of numerical errors related to the spatial resolution. Finally, we will illustrate model behavior for more complicated conditions by considering spectral evolution for turning winds.

In the above experiments, the new model is also compared with the most recent version of WAM [cycle

4 as described by Komen et al. (1994)]. For this comparison, two minor modifications have been made to WAM. First, propagation in north–south directions has been disabled to represent Eq. (1). Second, the frequency resolution, which cannot be changed externally in WAM, has been modified where necessary.

Figure 7 shows mean wave parameters as a function of the fetch $\tilde{x}$ for the numerical and physical conditions used in the previous section. To include conditions with extremely long fetches, additional runs have been performed with a grid with $\Delta x = 250$ km. Although the corresponding total fetch of 9500 km is unrealistic for the wind speed of 20 m s^{-1}, the nondimensional results are relevant for more common lower wind speeds. The parameters presented are the nondimensional energy $\tilde{E}$, peak frequency $\tilde{f}_p$, drag coefficient at 10-m height C_{10}, and the nondimensional energy level in the parametric tail $\alpha(f_c)$. The peak frequency is estimated from the one-dimensional spectrum $\mathcal{F}(f)$ using a parabolic fit for the three discrete frequencies around the discrete peak frequency.

Results of the new model tuned to the stable or unstable stratification data are represented by the solid and the dashed lines in Fig. 7. The nondimensional energy $\tilde{E}$ (panel a) shows excellent agreement with Eqs. (39) and (40) (not presented in figure) and with the corresponding data (shaded areas). The corresponding peak frequencies $\tilde{f}_p$ (panel b) are in reasonable agreement with the data but are 5%–10% higher than expected from (39) and (40). The drag coefficient C_{10} (panel c) shows the expected increase with decreasing fetch $\tilde{x}$. The nondimensional energy $\alpha(f_c)$ (panel d) for the model tuned to the stable data (solid line) shows excellent agreement with Eq. (41) and equals the Pierson–Moskowitz (1964) level for extremely long fetches. The results for the model tuned to the unstable data (dashed lines) shows some deviation from Eq. (41), but the results are still fairly good. The smooth model behavior and the consistency between results with all three resolutions indicate that the new model is fairly insensitive to numerical errors. Effects of numerical errors in the first few grid points are most pronounced in α (panel d) and to a lesser extend in $\tilde{f}_p$ (panel b).

Results of WAM are represented by the dotted lines in Fig. 7. For the long and extremely long fetch runs (center and right curves), the energy $\tilde{E}$ is similar to the results of the new model tuned to the unstable stratification data (panel a). The peak frequency $\tilde{f}_p$ (panel b) is lower than for the new model and is close to (40). The drag coefficient C_{10} shows a similar trend as the new model, and α is similar to α of the new model (panels c and d). For the short-fetch run (left lines), however, WAM greatly underestimates $\tilde{E}$ and shows aphysical behavior for C_{10} and α. This behavior is apparently due to correctable numerical errors in WAM (Janssen, oral presentation at WISE meeting in Venice, Italy, 1996).

Figure 8 shows one-dimensional energy spectra $\mathcal{F}(f)$ and nondimensional energy levels $\alpha(f)$ for several fetches $\tilde{x}$ as obtained from the model with $\Delta x = 25$ km tuned to the stable stratification data. The one-dimensional spectra show the expected behavior, with a small "overshoot" for the spectral peak of the younger waves. The nondimensional energy level α in Fig. 8b illustrates the existence of this overshoot (i.e., the local maximum of α at the peak of the spectrum) and shows that the overshoot decreases with decreasing peak frequencies. However, α also shows a local peak in the transition zone between the high- and low-frequency dissipation ($1.75–2.5 f_p$). This behavior is an artifact of the model. Because the magnitude of this maximum depends on the strength of the DIA (figures not presented here), we assume that this behavior is related to the artificially strong peak in the DIA for this frequency range (see Hasselmann et al. 1985, Fig. 7).

Figures 9 and 10 show the corresponding two-dimensional spectra and source terms for the shortest ($\tilde{x} = 1.05 \times 10^6$) and longest fetches ($\tilde{x} = 1.05 \times 10^7$), respectively. In both cases, the spectra show the smallest directional spread near the peak frequency. For short fetches (Fig. 9), the wind source term is entirely positive. The maximum input coincides with the spectral peak. Most of the input, however, occurs at frequencies well above the spectral peak. The dissipation source term roughly behaves opposite to the input and appears coherent and continuous in spite of its independent constituents. The nonlinear interactions shift energy to frequencies below the spectral peak and away from the wind direction for frequencies well above the spectral peak. Energy is removed from frequencies above the spectral peak for directions close to the wind direction. The net source term shows growth for frequencies around and below the spectral peak, and a net dissipation for frequencies just above the spectral peak. For frequencies well above the spectral peak, the source terms are approximately in balance. In the parametric tail (rightmost side of the panel, a small imbalance of the source terms can be observed. For large fetches (Fig. 10) the behavior of the source terms is qualitatively similar. The main difference with the short fetch results is that the source terms are more closely in balance and that the input becomes negative for low frequencies away from the wind direction. In this case the magnitude of the negative input is approximately 20% of the corresponding maximum of the nonlinear interactions. For even longer fetches (figures not presented here), the relative importance of the negative input increases, and eventually negative input occurs even for wave components traveling in the wind direction.

The second set of tests has been performed with a spectral discretization using 24 directions ($\Delta\theta = 15°$) and 25 frequencies (0.0418–0.412 Hz). This spectral resolution has been used in many WAM applications. The use of a preset spectral resolution implies that the actual windsea spectrum might be (partially) outside

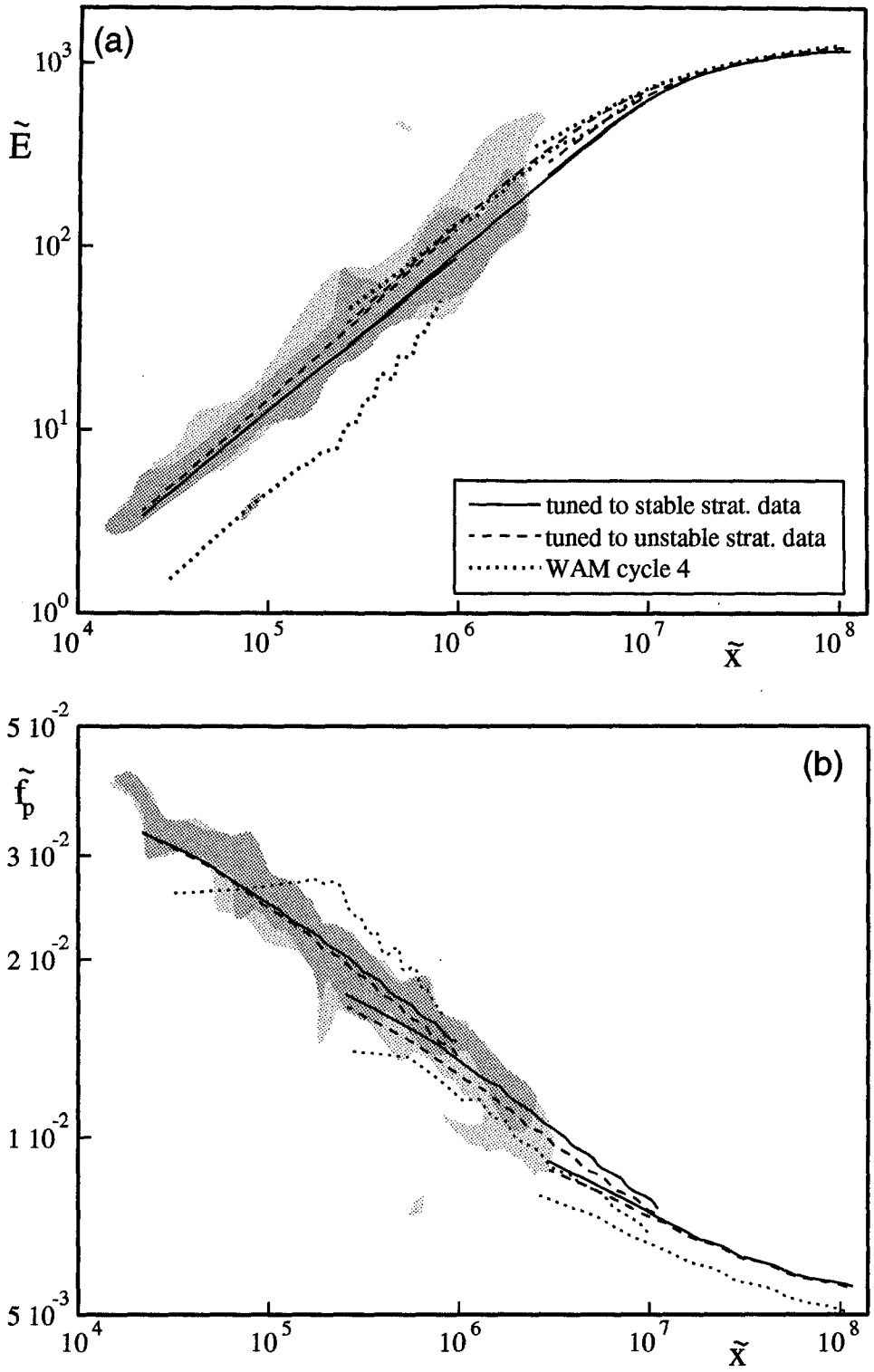

FIG. 7. Nondimensional energy $\tilde{E} = Eg^2u_*^{-4}$ (panel a), peak frequency $\tilde{f}_p = f_p u_* g^{-1}$ (panel b), the drag coefficient at 10 m $C_{10} = \sqrt{u_*/u_{10}}$ (panel c), and high-frequency energy level $\alpha(f_c)$ (panel d) as a function of the nondimensional fetch $\tilde{x} = xgu_*^{-1}$ for the conditions in which the model has been tuned and an additional

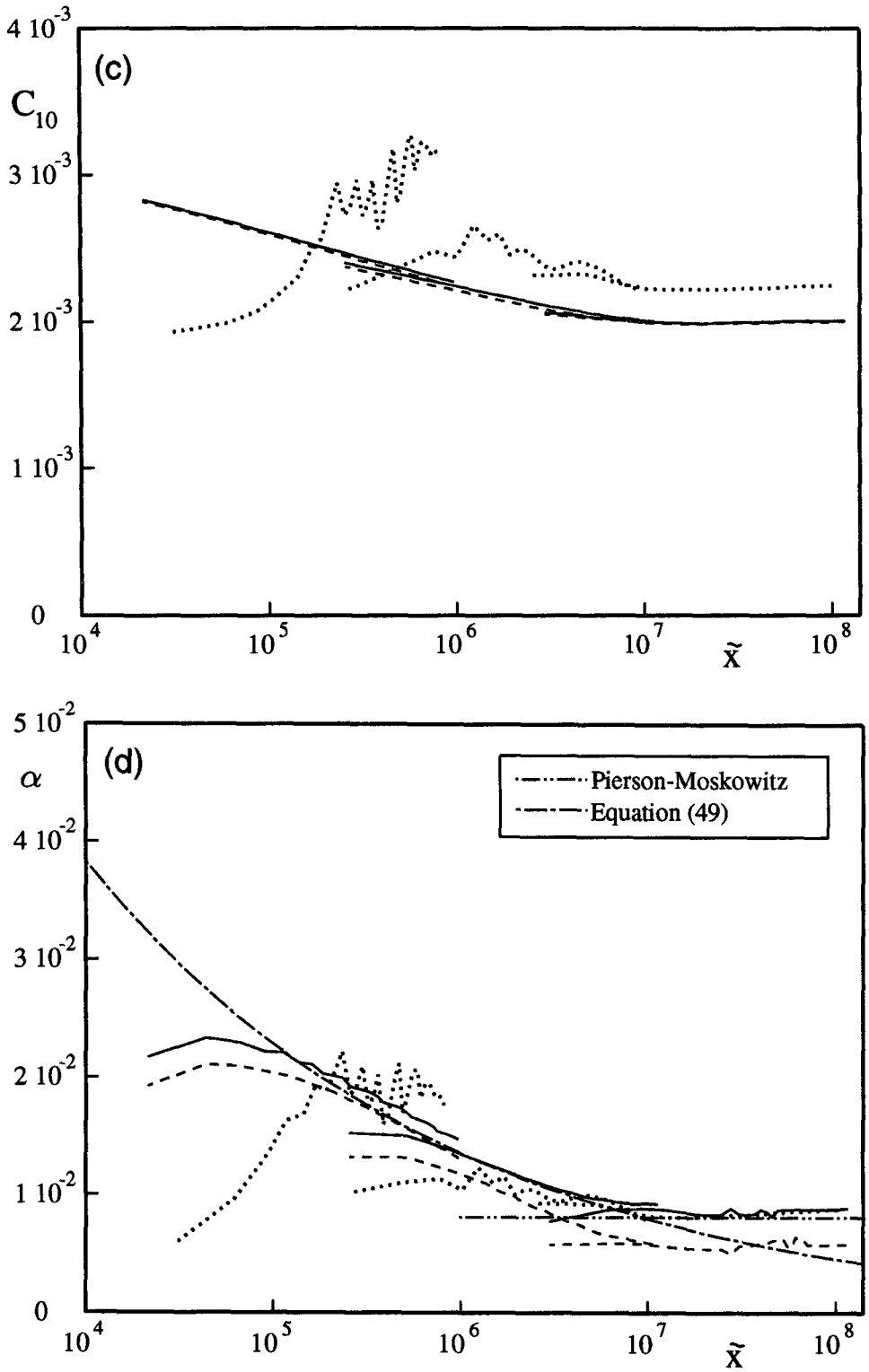

FIG. 7. (*Continued*) long-fetch case (Δx = 2.5, 25, and 250 km, respectively). The dark-shaded areas represent the envelope of the stable stratification data of Kahma and Calkoen (1992, 1994); the light represents all data.

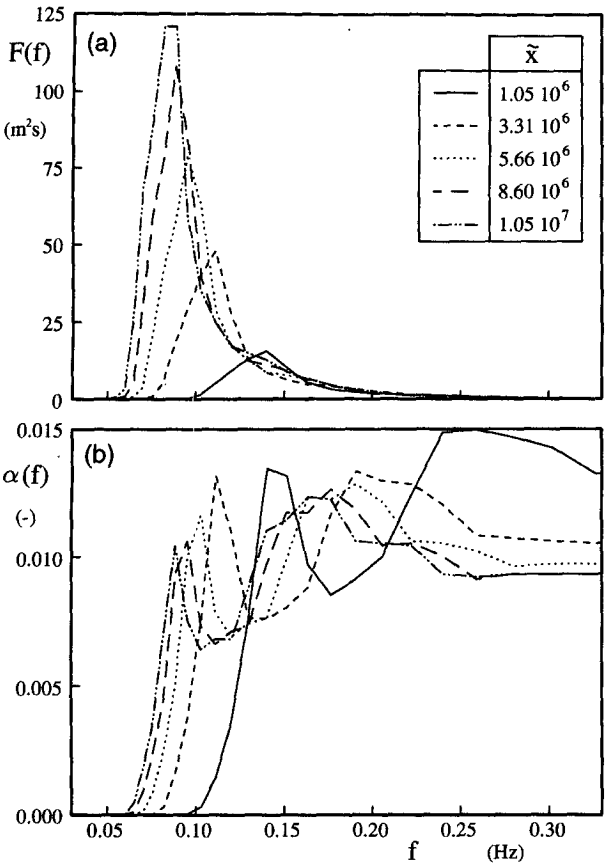

FIG. 8. One-dimensional energy spectra $\mathcal{F}(f)$ (a) and nondimensional energy level $\alpha(f)$ [Eq. (26)] (b) for several fetches $\tilde{x}$ corresponding to the growth curves of Fig. 7 (model tuned to stable stratification data, $\Delta x = 25$ km).

the discrete spectral range, in particular for low wind speeds. In such conditions the frequencies f_1, f_2, f_c, and f_h are larger than the maximum discrete frequency $f_{\max}$. In our numerical model we will allow this to happen, effectively removing the high-frequency dissipation and transition zones as shown in Fig. 3. Special attention has to be given to the length scale h in Eq. (23). To assure that the dissipation is not overestimated for poorly resolved spectra, Eq. (23) has to be evaluated within the parametric tail for the proper estimate of f_h.

Growth curves $\tilde{E}(\tilde{x})$ for wind speeds u_{10} ranging from 5 to 35 m s^{-1} are presented in Figs. 11 and 12. Figure 11 shows results normalized in terms of the friction velocity u_*. The new model tuned to the stable stratification data (panel a) shows excellent scaling behavior for wind speeds greater than 10 m s^{-1}, indicating that the new model is insensitive to numerical errors in this range of wind speeds and for the common discretizations presently used in third-generation models. For extremely low wind speeds the scaling behavior breaks down. This is caused by the fact that the corresponding spectrum is outside the discrete frequency range of the model. As the corresponding wave heights are small, this is not expected to have a significant impact on practical implementations. Scaling behavior for low wind speeds can be improved by extending the discrete frequency range to higher frequencies (Tolman 1992).

The WAM model (panel b) shows consistent scaling behavior for all wind speeds, with an underestimation of the wave energy for the smallest fetches (consistent with shortest fetches in Fig. 7a and likely due to a correctable numerical error). For higher wind speeds, results for the first few grid points deviate significantly, suggesting that WAM is more sensitive to numerical errors than the new model. The results of WAM are furthermore somewhat noisy. We suspect that this is due to the calculation of the wave drag from the high-frequency part of the spectrum, which is inherently noisy. A detailed investigation of its source, however, is outside the scope of the present paper.

Figure 12 shows the same results as Fig. 11, made nondimensional with the wind speed instead of the friction velocity. These results are not expected to scale as the relation between u_{10} and u_* depends on the wind speed. The results for the new model (panel a) show a significant dependency of the results on the wind speed. The results, however, are in good agreement with the observations, considering that the observations were made in wind speeds of 5–15 m s^{-1}. The results of WAM (panel b) are somewhat higher than the data for stable stratification (shaded area) but represent the results for unstable stratification well (not shown in figure). Surprisingly, the results of WAM appear to be approximately scaling with the wind speed for short fetches.

Finally, we will discuss qualitatively the results for a case with homogeneous wind conditions and a change in wind direction as an indication of the capability of the new model to handle more complex wave conditions. We consider a case similar to the turning wind case of Hasselmann et al. (1985). Starting from a small spectrum, we allow the wave field to grow for 12 hours under the influence of a wind with $u_{10} = 20$ m s^{-1}. After 12 hours, the wind turns instantaneously by 90° while maintaining its strength. Spectra just before and after the turning of the wind are presented in Fig. 13, and corresponding source terms are presented in Fig. 14.

After the wind shift, a windsea starts building at high frequencies in the new wind direction (Fig. 13). The old windsea, which is now swell, loses high-frequency energy quickly and low-frequency energy slowly. The wind "input" source term accounts for a large part of the swell dissipation, as can be observed in Fig. 14. The amount of dissipation of swell energy due to the interaction with the wind increases with increasing angle between the swell component and the wind. Due to this mechanism, the swell field appears to turn in the wind direction (Figs. 13c,d). Note that the nonlinear interactions keep shifting swell energy to lower frequencies and effectively slow down the shift in wave

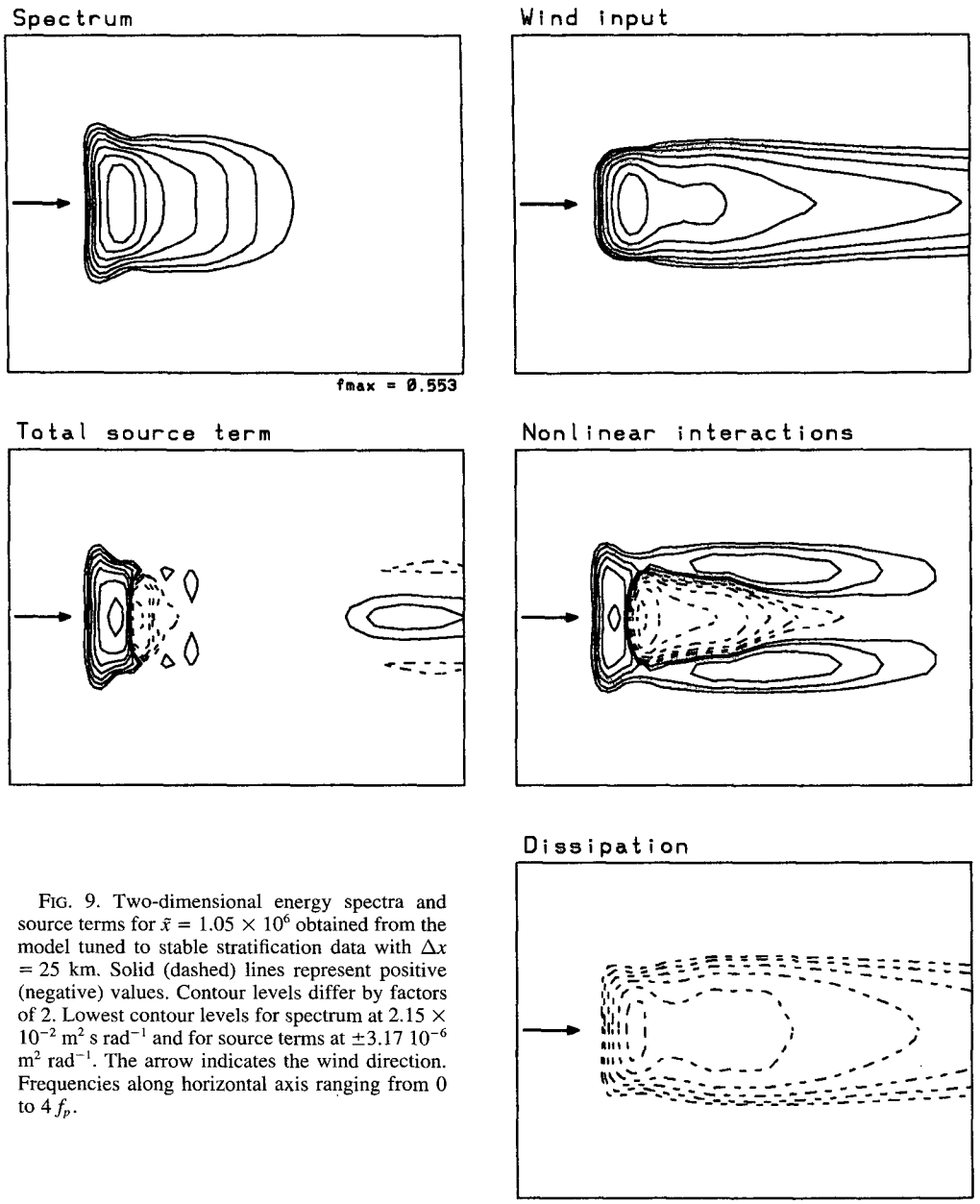

FIG. 9. Two-dimensional energy spectra and source terms for $\tilde{x} = 1.05 \times 10^6$ obtained from the model tuned to stable stratification data with $\Delta x = 25$ km. Solid (dashed) lines represent positive (negative) values. Contour levels differ by factors of 2. Lowest contour levels for spectrum at 2.15×10^{-2} m^2 s rad^{-1} and for source terms at $\pm 3.17\ 10^{-6}$ m^2 rad^{-1}. The arrow indicates the wind direction. Frequencies along horizontal axis ranging from 0 to $4 f_p$.

direction induced by the wind (see Van Vledder and Holthuijsen 1993).

7. Discussion

The present paper presents new parameterizations of the source terms for a third-generation ocean wave model. These parameterizations have been developed and tested for idealized fetch-limited conditions. An input source term is used that deviates significantly from the input terms as used in WAM. In spite of these differences, excellent growth behavior was obtained from extremely short fetches up to fully developed wave conditions. For intermediate and long fetches ($\tilde{x} > 10^6$), the new model and WAM show similar results (Fig. 7), although the choice of the dataset to which the new model is tuned leaves much room for adjustment in practical implementations [up to 40% in wave height, Kahma and Calkoen (1992, 1994)]. The new model also shows excellent results for extremely short fetches ($\tilde{x} < 2\ 10^5$), where WAM severely underestimates the wave energy (Figs. 7a and 11b), apparently

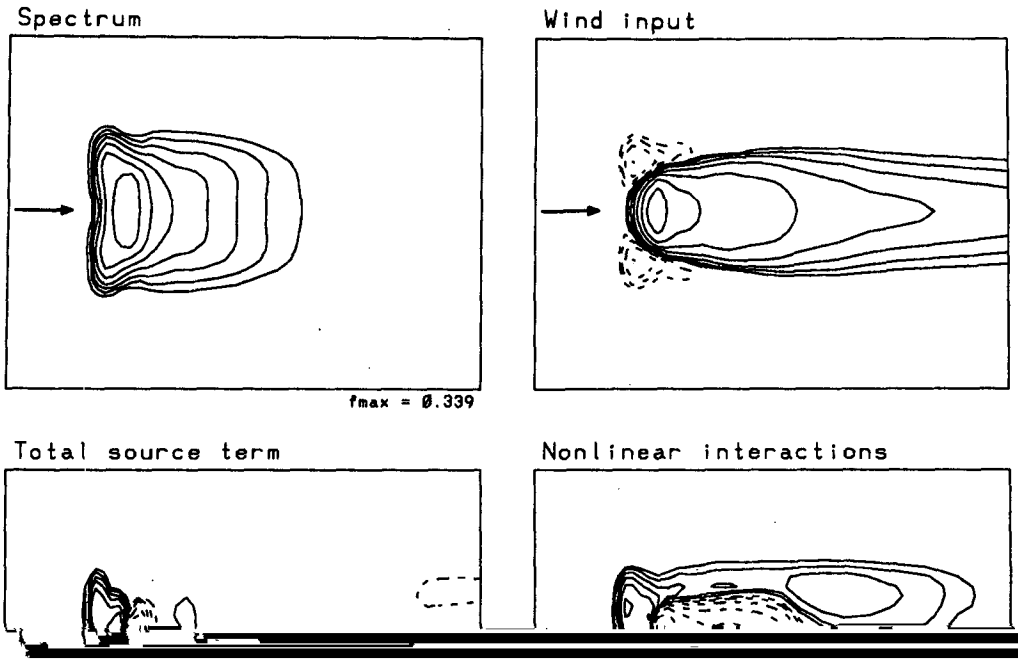
Spectrum
Wind input
fmax = Ø.339
Total source term
Nonlinear interactions

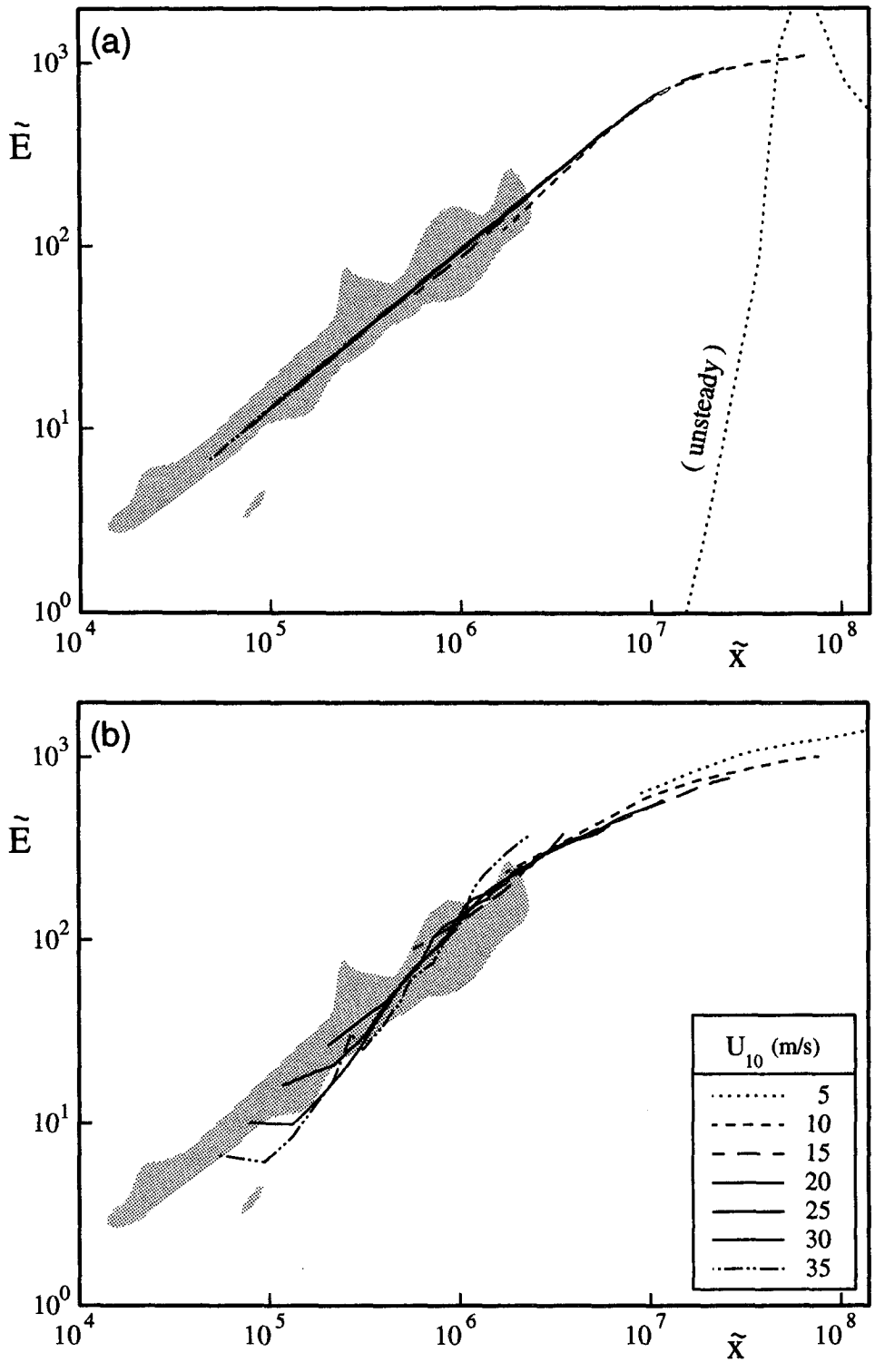

FIG. 11. Nondimensional energy $\tilde{E}$ as a function of the nondimensional fetch $\tilde{x}$ for various wind speeds. (a) New model tuned to stable stratification data. (b) WAM cycle 4. The shaded area represents the envelope of the stable stratification data of Kahma and Calkoen (1992, 1994). Δx = 25 km, $\Delta\theta$ = 15°, $\Delta f = 0.1f$ (0.0418–0.412 Hz).

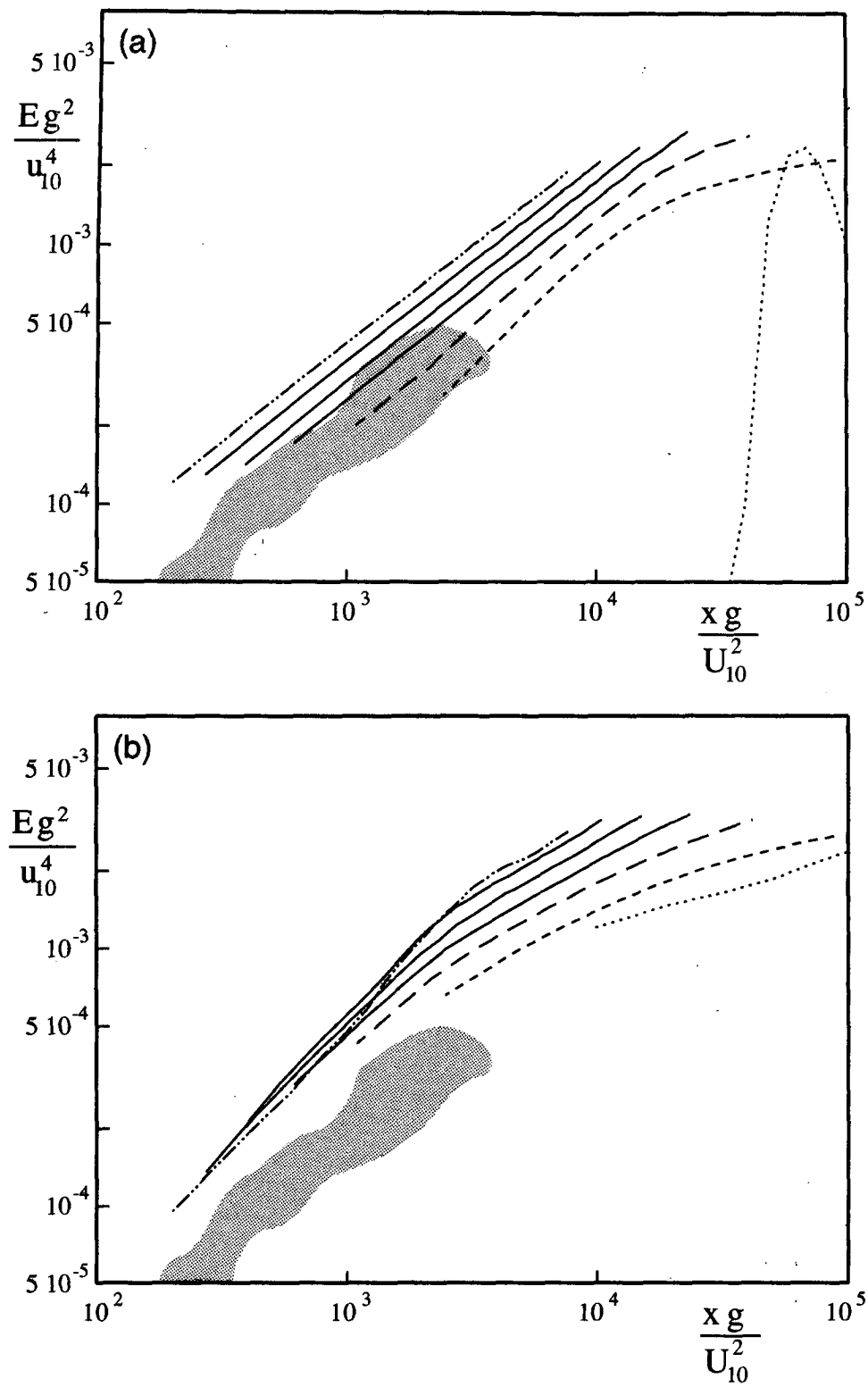

FIG. 12. As in Fig. 11 with nondimensional parameters in terms of the wind speed u_{10} instead of the friction velocity u_*.

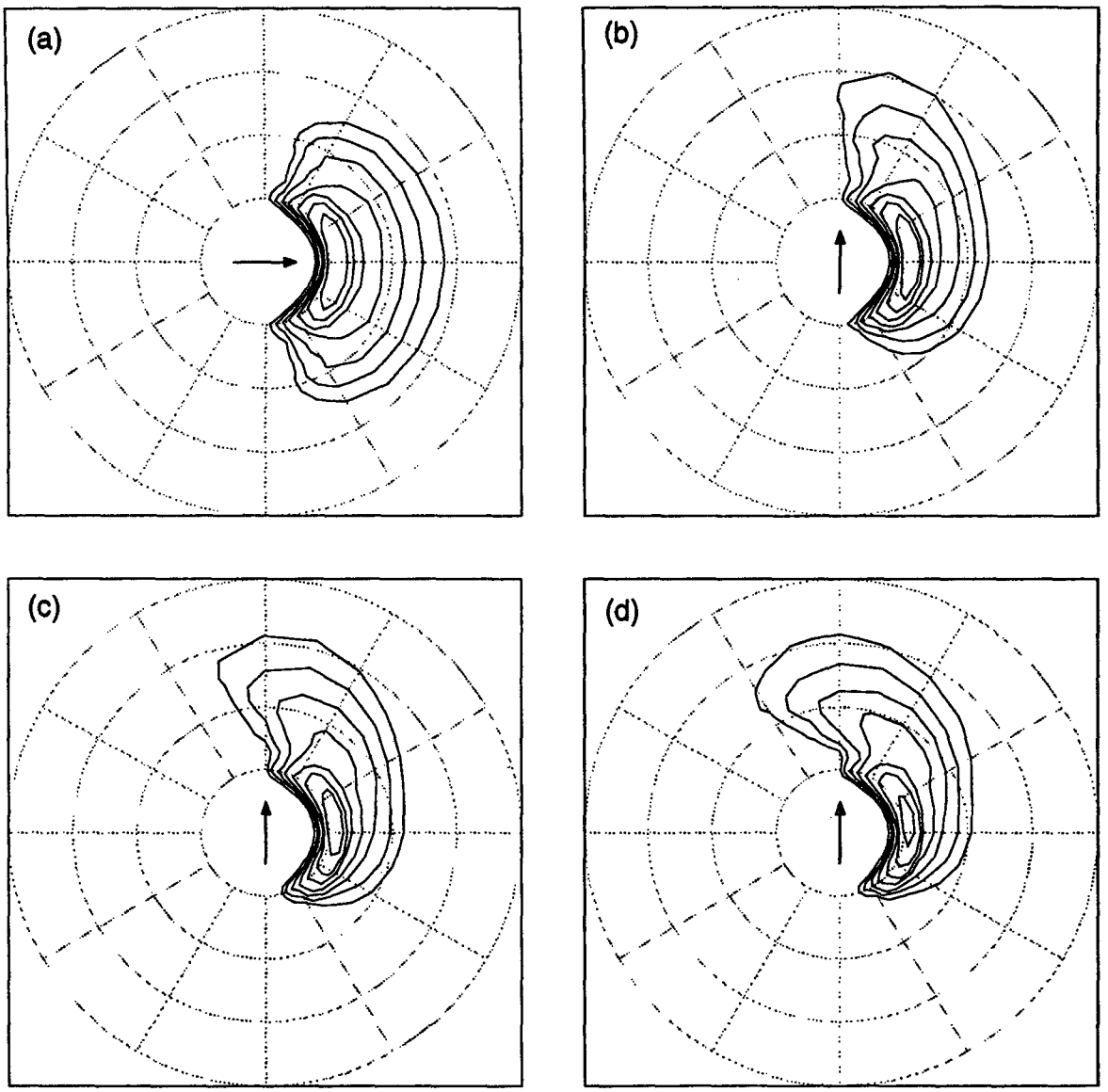

FIG. 13. Model response to a wind shift of 90°. (a) Spectrum just before wind shift and (b)–(d) spectra 1, 2, and 3 h after wind shift: $u_{10} = 20$ m s^{-1}. Lowest contour levels at 0.2 m^2 s rad^{-1}. Outermost grid circle corresponds to 0.4 Hz.

in a natural way from the input source term, whereas WAM estimates this frequency from the mean frequency of the entire spectrum (section 4c). Our approach results in more realistic model behavior, as is illustrated with the turning wind case presented in Figs. 13 and 14. After the turning of the wind, a new wind wave field is expected to grow at high frequencies in the wind direction. Equations (36) and (37) result in such behavior, as the transition to the parametric tail (f_c) is moved to high frequencies. If, however, f_c is related to the mean frequency as in WAM, the location of the parametric tail is governed by the swell field traveling in the old wind direction, and the new wind wave field cannot start its development at realistically high frequencies.

In the present model the stress is calculated using a parametric relation, which assumes a pure windsea without swell. Steep swells, however, can contribute appreciably to the total stress (Chalikov and Belevich 1993), which impacts both our input and dissipation. This problem could be solved by considering a hybrid algorithm, where the stress carried by the equilibrium range of the spectrum is calculated parametrically and where the remaining stress is calculated directly from the input source term. Note that the uncertainties in the calculated directional distribution for high frequencies (section 3), and unrealistic model behavior of $\alpha(f)$ for relatively high frequencies (Fig. 8b), support our arguments that the stress carried by the corresponding

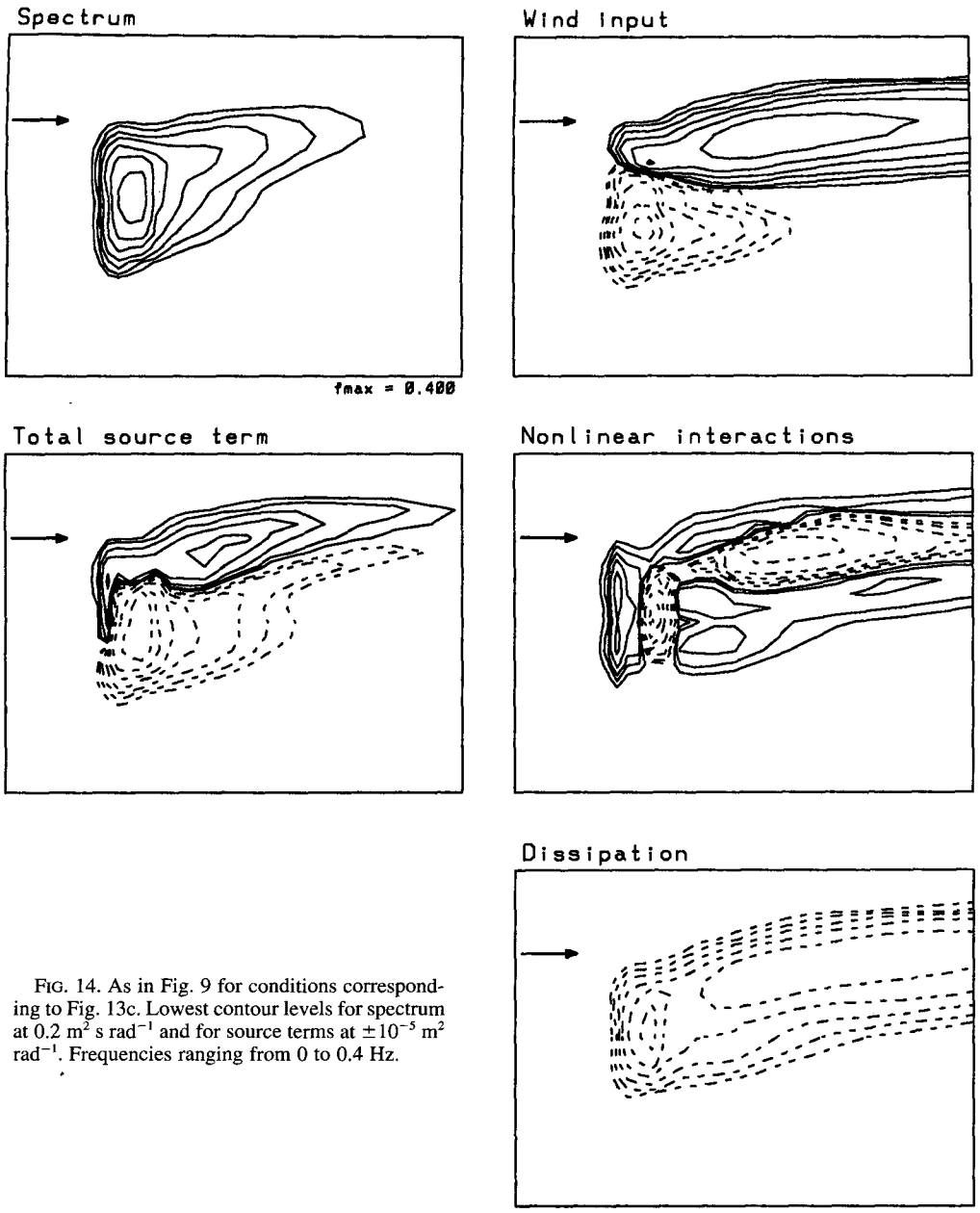

FIG. 14. As in Fig. 9 for conditions corresponding to Fig. 13c. Lowest contour levels for spectrum at 0.2 m^2 s rad^{-1} and for source terms at $\pm 10^{-5}$ m^2 rad^{-1}. Frequencies ranging from 0 to 0.4 Hz.

part of the spectrum should not be calculated directly from the input source term.

The present model has been developed assuming deep water conditions, for which the energy balance equation is given by (1). Generalization of Eq. (1) for limited water depths requires a modification of the present source terms and several other modifications (see, for instance, WAMDIG 1988). The physics of the input source term are governed by the shape of the surface and the propagation velocity of the waves. Limited water depths influence wave growth as they influence the phase speed of the waves. This effect can be incorporated in the input source term by replacing the nondimensional frequency $\tilde{\omega}_a$ (4) with a inverse nondimensional phase speed or "wave age"

$$\tilde{\omega}_a = \frac{u_\lambda}{c} \cos(\theta - \theta_w), \tag{44}$$

which for deep water is identical to Eq. (4). The nonlinear interactions can be adapted to limited water depths using a simple depth-dependent scaling (Hasselmann and Hasselmann 1985). The high-frequency dissipation does not require adaptations, as

water depths will be deep for this part of the spectrum in all but extremely depth-limited wind seas. The low-frequency dissipation has been expressed in terms of the wave geometry (wavenumber and spectral densities) and is therefore expected to be equally valid in deep water and in limited water depths.

In spite of the apparent success of our model, the problem of modeling the physics of growth of wind waves remains far from being resolved. All three source terms incorporate unresolved problems.

The input source term appears to be reasonably well established. Nevertheless several issues are still unresolved. For instance, the present wind–wave interaction parameter β is rather sensitive to the boundary conditions and the closure scheme of the Reynolds model on which it is based (e.g., Li et al. 1994). This adds an appreciable uncertainty to the Eqs. (3). Furthermore, direct observations of β exhibit large scatter, which makes a direct validation of an input source term practically impossible (e.g., Hasselmann and Bösenberg 1991). Finally, the input depends critically on the wind stress, which is governed mainly by the high-frequency range of the spectrum. This part of the spectrum cannot yet be modeled satisfactorily (from either a physical or a numerical perspective).

The nonlinear interactions are fairly well known, but economical considerations do not allow for a full parameterization in prediction models. Presently, the DIA is the only feasible parameterization of the nonlinear interactions for operational models. The original development of the DIA has concentrated on modeling the shift of wave energy to lower frequencies. The shift of energy to high frequencies, however, is modeled poorly (see section 3), which has implications for the modeling of the spectral shape at high frequencies (section 3 and Fig. 8b). Because many physical processes are concentrated at high frequencies (generation of stress and a large part of input and dissipation, e.g., see Fig. 9), this deficiency of the DIA deserves additional attention. It is interesting to observe, that our *decrease* of the strength of the DIA might be expected to decrease the growth rate of the waves because it decreases the shift of energy to lower frequencies. Instead, it results in an *increase* of the growth rate, as less input energy is shifted to higher frequencies, where it is dissipated and cannot contribute to wave growth (figures not presented here).

The physics of wave energy dissipation are still largely unknown, and the dissipation source term is used here as a tunable closure term in the wave energy balance equation. The main contribution of the present study to understanding the wave energy dissipation is the distinction of two separate dissipation regimes dominated by incompatible dissipation timescales. The high-frequency dissipation covers only a fraction of the total spectral energy. It nevertheless should be modeled explicitly, to avoid that the high-frequency dissipation dictates the spectral shape of the main (low frequency) dissipation. This new insight will hopefully simplify theoretical investigation into the spectral signature of whitecapping and other dissipation mechanisms.

The high-frequency dissipation source term presently has to be purely diagnostic, as we simply do not understand the complicated physics of the equilibrium range of the spectrum. Our high-frequency dissipation is directly derived from the other source terms, and can therefore not be expected to yield physical insight. For different parameterizations of S_{wind} and S_{nl}, and for different shapes of the parametric tail, the parameterization of high-frequency dissipation needs to be reassessed.

The choice to describe the low-frequency dissipation with a turbulence analogy is somewhat arbitrary. The dependence of this source term on the function ϕ makes the final definition of our source term to some extend a tuning exercise. A potential shortcoming of our low-frequency dissipation (25) is that it is directly related to the input through the friction velocity u_* and therefore vanishes for $u \to 0$. In such conditions steep swells will not be dissipated. The impact of this potential shortcoming should be investigated using realistic model implementations. Steep swells, however, are mostly due to strong effects of shoaling or due to wave–current interactions, both of which are expected to be relevant in relatively small-scale implementations only.

8. Conclusions

The present paper presents a new version of the third-generation ocean wave model WAVEWATCH using a wind input term based on Chalikov and Belevich (1993), the discrete interaction approximation (DIA) to nonlinear interactions and a new dissipation source term. It is suggested that the dissipation source term should consist of two constituents: Our high-frequency dissipation source term, applied near the equilibrium range of the spectrum, is purely diagnostic. Our low-frequency dissipation, which corresponds to the conventional whitecapping term, is based on an analogy with wave energy dissipation due to turbulence in the oceanic boundary layer.

The model is tuned and tested using standard fetch-limited growth conditions. Although our input source term is significantly weaker than previous input source terms, excellent growth behavior is obtained up to full development. However, details of the spectrum appear to be influenced significantly by errors in the DIA. The new model shows growth curves compatible to those of WAM cycle 4 for intermediate and long fetches, although the scatter in validation data leaves room for large modifications of the growth behavior. The new model also shows excellent growth characteristics for extremely small fetches, where WAM severely underestimates wave energy (apparently due to correctable numerical errors). The new model finally gives

smoother growth curves than WAM, and appears less sensitive to numerical errors.

Acknowledgments. The authors thank Charles Calkoen and Kimmo Kahma for supplying their data, and Paul E. Long Jr. and Willard J. Pierson for there useful comments on early drafts of this paper.

REFERENCES

Banner, M. L., and I. R. Young, 1994: Modeling spectral dissipation in the evolution of wind waves. Part I: Assessment of existing model performance. *J. Phys. Oceanogr.,* **24,** 1550–1571.

Benilov, A., and Y. Lozovatskii, 1977: Semi-empirical methods of the turbulent description of the ocean. *Coordination Center of COMECON (SEV),* Inf. Bull., **5,** 89–97.

Burgers, G., and V. K. Makin, 1993: Boundary-layer model results for wind-sea growth. *J. Phys. Oceanogr.,* **23,** 372–385.

Chalikov, D. V., 1980: Numerical simulation of the boundary layer above waves. *Bound.-Layer Meteor.,* **34,** 63–98.

——, 1995: The parameterization of the wave boundary layer. *J. Phys. Oceanogr.,* **25,** 1333–1349.

——, and V. K. Makin, 1990: Pressure distribution above waves. *Ann. Geophys.,* Special Issue, EGS, XV General Assembly, p. 198.

——, and M. Y. Belevich, 1993: One-dimensional theory of the wave boundary layer. *Bound.-Layer Meteor.,* **63,** 65–96.

Charnock, H., 1955: Wind stress on a water surface. *Quart. J. Roy. Meteor. Soc.,* **81,** 639–640.

Donelan, M., and Y. Yuan, 1994: Wave dissipation by surface processes. *Dynamics and Modelling of Ocean Waves,* G. J. Komen et al., Eds., Cambridge University Press, 143–155.

Gelci, R., H. Cazalé, and J. Vassal, 1956: Utilization des diagrammes de propagation à la prévision énergétique de la houle. Bulletin d'information du commité central d'océanographie et d'études des côtes 8, 169–197.

Hasselmann, D. E., and J. Bösenberg, 1991: Field measurements of wave-induced pressure over wind sea and swell. *J. Fluid Mech.,* **230,** 391–328.

——, M. Dunkel, and J. A. Ewing, 1980: Directional wave spectra observed during JONSWAP 1973. *J. Phys. Oceanogr.,* **10,** 1264–1280.

Hasselmann, K., T. P. Barnett, E. Bouws, H. Carlson, D. E. Cartwright, K. Enke, J. A. Ewing, H. Gienapp, D. E. Hasselmann, P. Kruseman, A. Meerburg, P. Müller, D. J. Olbers, K. Richter, W. Sell, and H. Walden, 1973: Measurements of wind-wave growth and swell decay during the Joint North Sea Wave Project (JONSWAP). *Erg. Dtsch. Hydrogr. Z.,* Reihe A (8), No. 12, 95 pp.

Hasselmann, S., and K. Hasselmann, 1985: Computations and parameterizations of the nonlinear energy transfer in a gravity-wave spectrum. Part I: A new method for efficient computations of the exact nonlinear transfer integral. *J. Phys. Oceanogr.,* **15,** 1369–1377.

——, ——, J. H. Allender, and T. P. Barnett, 1985: Computations and parameterizations of the nonlinear energy transfer in a gravity-wave spectrum. Part II: Parameterizations of the nonlinear energy transfer for application in wave models. *J. Phys. Oceanogr.,* **15,** 1378–1391.

Janssen, P. E. A. M., 1989: Wind-induced stress and drag of air-flow over waves. *J. Phys. Oceanogr.,* **19,** 745–754.

——, 1991: Quasi-linear theory of wind wave generation applied to wind wave forecasting. *J. Phys. Oceanogr.,* **21,** 1631–1642.

Kahma, K. K., and C. J. Calkoen, 1992: Reconciling discrepancies in the observed growth rates of wind waves. *J. Phys. Oceanogr.,* **22,** 1389–1405.

——, and ——, 1994: Growth curve observations. *Dynamics and Modelling of Ocean Waves,* G. J. Komen et al., Eds., Cambridge University Press, 174–182.

Kitaigorodskii, S. A., and Y. Z. Miropolskii, 1968: Dissipation of turbulent energy in the surface layer of the ocean. *Izv. Acad. Sci. USSR Atmos. and Oceanic Phys.,* **4,** 647–659.

——, and J. L. Lumley, 1983: Wave–turbulence interaction in the upper ocean. Part I: The energy balance of the interacting fields of surface wind waves and wind-induced three-dimensional turbulence. *J. Phys. Oceanogr.,* **13,** 1977–1987.

Komen, G. J., S. Hasselmann, and K. Hasselmann, 1984: On the existence of a fully developed wind-sea spectrum. *J. Phys. Oceanogr.,* **14,** 1271–1285.

——, L. Cavaleri, M. Donelan, K. Hasselmann, S. Hasselmann, and P. E. A. M. Janssen, 1994: *Dynamics and Modelling of Ocean Waves.* Cambridge University Press, 532 pp.

Li, Y. P., D. Xu, and P. P. Taylor, 1994: A non-linear numerical model of turbulent flow over water waves. *Proc. Waves—Physical and Numerical Modelling,* Vancouver, BC, Canada, University of British Columbia, 684–693.

Panchenko, H., and D. V. Chalikov, 1984: On measurements of energy and momentum input to the sea waves. *Izv. Atmos. Ocean Phys.,* **2,** 136–140.

Phillips, O. M., 1977: *Dynamics of Upper Ocean.* 2d ed. Cambridge University Press, 261 pp.

Pierson, W. J., and L. Moskowitz, 1964: A proposed spectral for fully developed wind seas based on the similarity theory of S. A. Kitaigorodskii. *J. Geophys. Res.,* **69,** 5181–5190.

Plant, W. J., 1982: A relationship between wind stress and wave slope. *J. Geophys. Res.,* **87,** 1961–1967.

Snyder, R. L., F. W. Dobson, J. A. Elliot, and R. B. Long, 1981: Array measurements of atmospheric pressure fluctuations above gravity waves. *J. Fluid Mech.,* **102,** 1–59.

——, L. M. Lawson, and R. B. Long, 1992: Inverse modelling of the action balance equation. Part I: Source expansion and adjoint model equations. *J. Phys. Oceanogr.,* **22,** 1540–1555.

SWAMP Group, 1985: *Ocean Wave Modelling.* Plenum Press, 256 pp.

SWIM Group, 1985: A shallow water intercomparison of three numerical wave prediction models (SWIM). *Quart. J. Roy. Meteor. Soc.,* **111,** 1087–1112.

Tolman, H. L., 1991: A third-generation model for wind waves on slowly varying, unsteady and inhomogeneous depths and currents. *J. Phys. Oceanogr.,* **21,** 782–797.

——, 1992: Effects of numerics on the physics in a third-generation wind-wave model. *J. Phys. Oceanogr.,* **22,** 1095–1111.

Van Vledder, G. P., and L. H. Holthuijsen, 1993: The directional response of ocean waves to turning winds. *J. Phys. Oceanogr.,* **23,** 177–192.

WAMDIG, 1988: The WAM model—A third generation ocean wave prediction model. *J. Phys. Oceanogr.,* **18,** 1775–1810.